Eindhoven University of Technology

MASTER

Homogeneous nucleation in methane/nonane mixtures at high pressures

Luijten, C.C.M.

*Award date:*
1994

Link to publication

# Technische Universiteit tu Eindhoven

Titel:

## Homogeneous nucleation in methane/nonane mixtures at high pressures

Auteur:                      C.C.M. Luijten

Verslagnummer:               R – 1303 – A

Datum:                       september 1994

Werkeenheid:        Gasdynamica/Aeroakoestiek

Afstudeerdocent:    dr. ir. M.E.H. van Dongen

Begeleiding:        ir. K.N.H. Looijmans

# Abstract

Homogeneous nucleation is the first stage of the dropwise condensation process in the absence of foreign particles, which occurs when a vapour is brought to a sufficiently high supersaturated state.

Condensation of natural gas at high pressures is of great interest to the oil and gas industry. Since a binary mixture of $n$-nonane and methane shows similar phase behaviour as natural gas, the present investigation has concentrated on the nucleation behaviour of this mixture.

The classical binary nucleation theory has been reviewed and extended with a real gas model for the formation free energy of droplets based on the Redlich-Kwong-Soave equation of state. The model predicts a large influence of methane on the nucleation of the binary mixture. Calculated nucleation rates increase by several orders of magnitude upon a 10 bar increase of total pressure when supersaturation is fixed. This is a result of the increasing solubility of methane in the liquid phase at high pressures, which reduces the surface tension of the formed nuclei and thereby the formation free energy barrier. At the same time, for a fixed nonane density, the nucleation rate decreases with pressure because of the increasing solubility of nonane in the vapour phase.

The expansion shock tube device used for measuring nucleation rates and droplet growth rates has been adapted for use at high pressures. In this setup a pulse-like supersaturation is created, which enables counting and sizing of the droplets by optical means (transmitted light extinction and 90° Mie-scattering measurements). Gas compositions have been determined on the basis of a sampling method and by means of comparison to an existing growth model. The sampling method systematically yields larger values for the nonane concentration than the growth method.

Experiments on the nucleation behaviour of the $n$-nonane/methane mixture have been performed at pressures up to 40 bar. Critical supersaturations turn out to decrease with increasing pressure. The nucleation rate as a function of partial nonane density (when calculated with the growth method) turns out to be approximately independent of pressure. The same conclusion holds for measurements on the $n$-nonane/argon mixture at pressures near 20 bar, but the critical values for the partial nonane density are lower in this case.

Since the two methods used for determining the composition of the nucleating mixture have not yet been proven to be sufficiently reliable at high pressures, it is not clear if these observations can be attributed to real gas effects.

# Contents

# Chapter 1

# Introduction

Homogeneous condensation, the formation of droplets out of a supersaturated vapour, can be observed in a variety of situations, both in everyday's life and in technical environments. In nature, fog can be formed when the temperature of a humid atmosphere quickly decreases. Another well-known example is the opening of a bottle of beer: when the stop is removed, mist is formed due to the sudden expansion of the saturated air on top of the liquid in the bottle. A technical application of condensation is found in a gas purification plant: as a result of sudden pressure drops, the gas is cooled down and a state of supersaturation can be reached, resulting in droplet formation. This effect can be used as a helpful tool in the purification process. It may not be desired, however, because the liquid formed can obstruct the gas flow through pipes or valves.

All these examples share an important feature: the gas is brought into a thermodynamic non-equilibrium state by means of a relatively fast cooling, in most cases combined with an expansion. This immediately provides us with a tool for the study of condensation in the laboratory, as we will see later on in this text. The condensation process decreases the density of vapour molecules (thereby the supersaturation $S$), so it is in fact the way back to equilibrium. This is illustrated in figure 1.1.
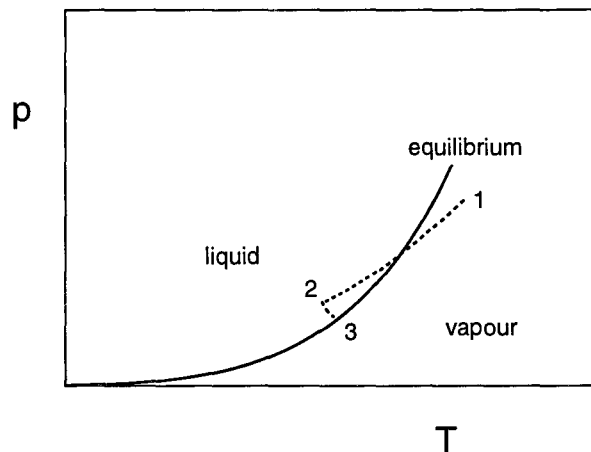
Figure 1.1: *Schematic phase diagram of a pure vapour (solid line). Dashed line indicates the history of thermodynamic states during undercooling (1 $\rightarrow$ 2) and condensation (2 $\rightarrow$ 3).*

The condensation process consists of two stages: nucleation, being the formation of microscopic clusters from the vapour phase (with radii of the order of nanometers), and droplet growth, whereby the microscopic clusters grow to macroscopic – optically detectable – sizes. When foreign particles (condensation nuclei) are added, only the growth stage is present; the condensation is called heterogeneous. We will only consider condensation in the absence of such particles. The formation of nuclei from the homogeneous vapour phase is then called homogeneous nucleation. This work will, as far as the theoretical part is concerned, concentrate on the nucleation process. The droplet growth process is extensively used in obtaining and interpreting experimental results.

As already remarked, condensation can only take place in a supersaturated vapour. Moreover, the supersaturation (which is, in its generally used definition, the ratio of the vapour pressure to the saturated vapour pressure at the same temperature) has to reach some critical value in order for the condensation process to occur (obviously, this critical value has to be larger than unity).

The cause of this is found in the nucleation process. Owing to thermal density fluctuations in the vapour, there always exists some equilibrium number distribution of clusters in the system as a function of cluster size. This distribution is proportional to a Boltzmann factor $\exp\left(-\Delta G_n/k_B T\right)$. $\Delta G_n$ denotes the free energy of formation of a cluster consisting of $n$ molecules, $k_B$ is Boltzmann's constant and $T$ is temperature. In the classical nucleation theory, an important concept is the capillarity approximation: properties of microscopic clusters are taken as if the clusters were macroscopic liquid droplets. In this model, the free energy of formation of these clusters consists of two terms. One term is negative and proportional to $n$; it represents the energy gain upon formation of bulk liquid (energetically favourable in a supersaturated vapour). The other term is positive and results from the fact that formation of the surface costs energy. It is therefore proportional to the surface area (and thus to $n^{2/3}$). The net result is, that the formation free energy exhibits a maximum as a function of cluster size. Clusters that consist of the number of molecules for which the maximum is attained are called critical clusters or nuclei. In this way an energy barrier is constituted; clusters that contain less molecules than the critical nucleus tend to evaporate, whereas larger clusters tend to grow to macroscopic sizes. The nucleation rate $J$ – which is the number of droplets formed per unit time and unit volume – is proportional to the number density of critical nuclei, and thus to the factor $\exp\left(-\Delta G_{crit}/k_B T\right)$.

From a technical point of view, condensation of natural gas is of great interest in the oil and gas industry. This problem is a great deal more complicated than that of condensation in a pure vapour, because natural gas consists of many components. The phase behaviour of a multi component system is essentially different from the single component case: there is no single vapour-liquid equilibrium line, but there is a lob-formed coexistence region in which the two phases can mutually exist. A schematic representation of this phenomenon is given in figure 1.2. From this figure, it is clear

that a lowering of total pressure can result in condensation of the mixture, which is then called retrograde condensation.
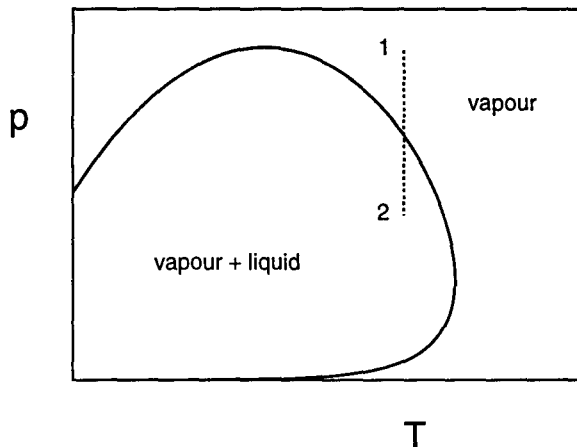


Figure 1.2: *Schematic phase diagram of a mixture of alkanes of fixed composition (solid line). Dashed line indicates the history of thermodynamic states during an isothermal expansion* $(1 \rightarrow 2)$.

A binary mixture of methane and one heavier alkane, for instance $n$-nonane, is known to reproduce this phase behaviour in the pressure and temperature range of interest, in the sense that its phase envelope largely coincides with that of natural gas. Experiments have therefore focussed on this mixture.

The retrograde behaviour is a typical real gas effect, and is not expected to be observed for all mixtures: when an inert gas is mixed with nonane vapour, its role is expected to be restricted to raising the pressure, and the inert gas molecules will not be present in the liquid phase. The vapour-liquid line of nonane can be slightly shifted, but no phase envelope is present. This distinction leads to some differences in condensation behaviour. In order to investigate these, some experiments on $n$-nonane/argon mixtures were performed. However, in the course of this work, argon turned out not to behave like an inert gas in the above described sense.

The theoretical description of nucleation in binary mixtures is much more complicated than in the single component case: the critical nucleus can contain both components. The formation free energy of clusters is no longer a simple function of cluster size, but constitutes a surface as a function of the numbers of molecules of the two components, $n_a$ and $n_b$. This is illustrated in figure 1.3. The free energy surface exhibits a saddlepoint, over which clusters have to pass in order to grow to macroscopic sizes. Along the $n_a$-axis $(n_b = 0)$, the situation in the single component case can also be recognized. Again, the nucleation rate is proportional to a Boltzmann factor $\exp\left(-\Delta G_{sp}/k_B T\right)$, in which now the formation free energy of the cluster represented by the saddlepoint is present.

Chapter 2 consists of an article in which the classical binary nucleation theory is critically reviewed and applied to nucleation of the mixture $n$-nonane/methane in the retrogade
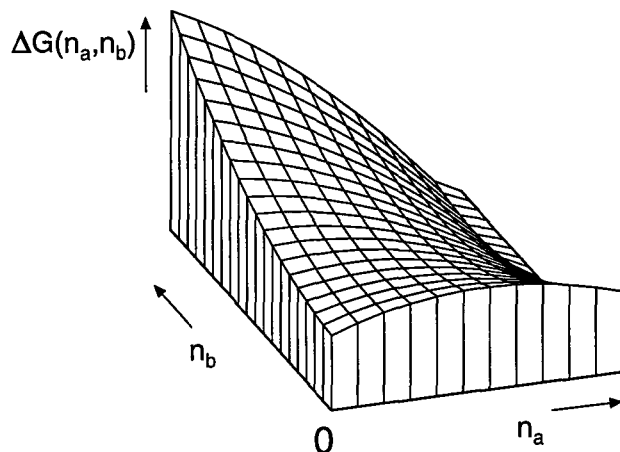
Figure 1.3: *Free formation energy of clusters as a function of the numbers of molecules $n_a$ and $n_b$ for a binary mixture.*

region.[1] A new aspect of our approach is the implementation of an equation of state into the calculations that accounts for real gas effects occurring in the $n$-nonane/methane mixture (and, more generally, in other alkane mixtures and thus in natural gas) at high pressures.

In chapter 3 attention is paid to the experimental technique that is used to determine nucleation rates at high pressures. In the group Gasdynamics and Aeroacoustics, department of Fluid Dynamics, Eindhoven University of Technology, two different devices for determining nucleation rates are used: a Wilson expansion cloud chamber and an expansion wave tube. All experiments in this work were performed with the latter. By means of a local widening in the tube, a pressure history is created at the endwall that causes a pulse-like supersaturation of the heavier component. The experiment can be designed in such a way that the peak value of supersaturation is just high enough to cause detectable condensation. Before and after the pulse no significant nucleation takes place, but the formed nuclei do grow to macroscopic sizes after the nucleation period. This process can be optically traced. Information about both nucleation and growth rates can be obtained in this way. The emphasis of the experimental work is on the determination of the thermodynamic state during the nucleation pulse: pressure, temperature and the vapour fraction of $n$-nonane in the mixture.

Experimental results are discussed in chapter 4. Of course, in order to check the nucleation model described in chapter 2, results are compared to calculations with the model.

In chapter 5 some conclusions will be drawn and recommendations given for future work in this field.

---

[1]The article has been submitted to the Journal of Chemical Physics at August 31, 1994.

# Nucleation theory

## Classical binary nucleation theory applied to the real mixture $n$-nonane/methane at high pressures

K.N.H. Looijmans*     C.C.M. Luijten     G.C.J. Hofmans

M.E.H. van Dongen

August 31, 1994

### Abstract

A thermodynamic model of the formation free energy of a droplet, based on a real equation of state, has been implemented in the binary classical nucleation theory to analyse homogeneous nucleation of mixtures of $n$-nonane and methane in the coexistence region at high pressures. The composition of the critical nucleus is computed by solving the Kelvin equations, the chemical potentials and molar volumes being evaluated from the RKS equation of state. Real gas behavior appears to have a strong effect on nucleation due to mutual interactions between methane and nonane molecules. Numerical calculations show an increasing concentration of methane in critical clusters with increasing pressure at fixed temperature and supersaturation. As a consequence, the surface tension of the critical droplets, which is evaluated by means of the Parachor method, is lowered, having a strong increasing effect on the nuclation rate: a 10 bar increase of total pressure leads to an increase of the nucleation rate of several orders of magnitude.

*Correspondence to: Eindhoven University of Technology, Faculty of Applied Physics, P.O. Box 513, 5600 MB Eindhoven, The Netherlands

# 1 Introduction

During handling and transport of natural gas, it is observed that large and sudden pressure drops may induce mist formation. Muitjens *et al.*[1] showed that the condensation in the gas mixture is a non-equilibrium phase change of the higher alkanes, such as nonane and decane, which are present in the mixture besides the main components methane and nitrogen. From the strong deviation from vapor–liquid phase equilibrium of the onset points of condensation measured in a Wilson cloud chamber, it was concluded that droplets were formed by a homogeneous nucleation process. The measured onset points were located inside the coexistence region of the gas mixture in the $p - T$ phase diagram, above the critical temperature of the main component methane. This coexistence region is characterized by the appearance of real gas effects in condensation, when pressure is above a few bars. The real gas effects become visible in density dependent solubilities affecting partial equilibrium vapor pressures, and in so–called retrograde condensation i.e. condensation induced by a decrease of pressure.

Up to now, no examples of application of nucleation theory to nucleation in the coexistence region at high pressures are known from literature. In this paper we present numerical calculations based on classical binary nucleation theory of the mixture methane/$n$-nonane. Since natural gas consists of many components, most of them being heavier hydrocarbons, we chose the methane/$n$-nonane mixture as a model mixture to study homogeneous nucleation. At pressures ranging from 10 bar to 200 bar, corresponding to exploration pressures of natural gas, the coexistence regions of natural gas and of the mixture mentioned above with a molar $n$-nonane concentration of about $10^{-4}$, largely coincide in the $p - T$ phase diagram and are therefore expected to exhibit similar real gas effects in condensation.

From now on, we shall consider the methane/$n$-nonane mixture. The real gas effects due to the mutual interactions of the nonane and methane molecules lead to a solubility of methane in liquid nonane that increases with pressure. Since the droplets will contain a significant amount of methane besides the nonane, the modeling of homogeneous nucleation requires a binary nucleation model.

The theory of homogeneous condensation goes back to the work of Volmer and Weber[2] and Becker and Döring[3]. They developed the Classical Nucleation Theory (CNT) of pure vapors which predicts the nucleation rate i.e. the rate at which critical nuclei are formed. A major role in this theory is played by the capillarity approximation: properties of microscopic droplets are taken as if the droplets were of macroscopic sizes. Reiss[4] extended CNT to binary vapors. The calculation of the kinetic prefactor was improved by Stauffer[5]. Later, the correctness of the implementation of the Gibbs-Duhem identity in binary nucleation theory was discussed by Renninger *et al.*[6], Doyle[7] and Wilemski[8]. Wilemski[8–10] introduced the model of a droplet consisting of a bulk and a surface layer with excess molecules[11,12], and at the same time pointed out the shortcomings of this model. Because of the rather unsatisfactory assumption of the capillarity approximation for droplets that consist of typically 10 to 100 molecules, several attempts have been made to improve CNT[13–16] with varying success.

Numerical studies of binary homogeneous condensation with CNT performed so far mainly refer to aqueous solutions and mixtures of alcohols. Nucleation rates were determined as a function of activities of the species present in the mixture, and attention was paid to the composition of the critical cluster[17]. In the following sections we will present an extension of CNT allowing calculation of nucleation rates in mixtures showing real gas effects. Results obtained with the model are presented.

## 2 Binary homogeneous nucleation theory

Since the introduction of binary nucleation theory, different models and interpretations have been published in the literature. Therefore we shall give a brief outline of the theory as it is implemented in our calculations.

The nucleation rate is the number of droplets formed per unit time and space. It is expressed in the following form:

$$J = K \cdot e^{-\Delta G/k_B T}. \tag{1}$$

$K$ is a kinetic prefactor, $\Delta G$ in the exponential is the free reversible energy of formation of a critical droplet, $k_B$ is Boltzmann's constant, and $T$ is the temperature. The energy of formation $\Delta G(n_1, n_2)$ is a function of the numbers of particles of species 1 and 2 in the droplet. When the gas-vapor mixture is in a supersaturated state, the $\Delta G(n_1, n_2)$ plane exhibits a saddlepoint. The position of this saddlepoint is considered to represent the critical nucleus. The critical nucleus is in unstable equilibrium with the surrounding vapor, and the saddlepoint forms the lowest passage over an energy barrier. Clusters passing over this barrier will grow to macroscopic droplets. Different models have been employed to calculate $\Delta G$. In CNT, Gibbs' capillarity approximation is used to describe the clusters on the basis of classical thermodynamics.

### 2.1 Classical droplet model

We adopt the binary classical theory as described by Wilemski. In this macroscopic model of a droplet and surrounding vapor, the droplet consists of bulk liquid with numbers of bulk molecules $n_1^l$ and $n_2^l$, and a surface layer with numbers of surface molecules $n_1^s$ and $n_2^s$. Bulk and surface are considered to be in thermodynamic equilibrium and the droplet is assumed to be incompressible. The number of surface molecules is an excess number, defined as $n^s = n - n^l - n^v$, where $n$ is the total number of molecules in the system, and $n^v$ is the number of molecules in the vapor. The excess molecules $n_i^s$ do not contribute to the droplet volume. The presence of the surface layer in the droplet model implicitly takes into account the effect of surface enrichment; the concentration of species 1 and 2 near the surface can differ from the interior composition. According to this droplet model, the free formation energy is[8]:

$$\Delta G = (p - p^l)V^l + \sigma A + \sum_{i=1,2} (\mu_i^l - \mu_i^v) n_i^l + \sum_{i=1,2} (\mu_i^s - \mu_i^v) n_i^s. \tag{2}$$

Chemical potentials $\mu_i^l$ and $\mu_i^v$ are evaluated at pressures $p^l$ in the droplet and $p^v$ of the vapor respectively. $V^l$ is the droplet volume. Because bulk liquid and surface are assumed to be in equilibrium, $\mu_i^s = \mu_i^l$, and therefore bulk and surface molecules can be taken together in Eq. (2): $n_i^t = n_i^l + n_i^s$. If we define the difference in chemical potential between droplet and vapor as $\Delta\mu_i = \mu_i^l(p^l, T) - \mu_i^v(p^v, T)$, and furthermore assume that the formation of clusters does not lead to a change of vapor pressure $p$ (i.e. $p^v = p$), then $\Delta G$ can be written as

$$\Delta G = (p^v - p^l)V^l + \sigma A + \sum_{i=1,2} \Delta\mu_i n_i^t. \tag{3}$$

The saddlepoint of this $\Delta G$ plane is determined by

$$\left.\frac{\partial \Delta G}{\partial n_i^t}\right|_{sp} = 0, \quad i = 1, 2. \tag{4}$$

Combining Eqs. (3) and (4) together with the Gibbs-Duhem relation for the bulk,

$$S^l dT - V^l dp^l + \sum_{i=1,2} n_i^l d\mu_i^l(p^l, T) = 0, \tag{5}$$

and the Gibbs adsorption equation for the surface,

$$S^s dT - A d\sigma + \sum_{i=1,2} n_i^s d\mu_i^s = 0, \tag{6}$$

we arrive at:

$$\Delta\mu_i = 0. \tag{7}$$

In deriving the last result, we used the Laplace relation $p^l = p^v + 2\sigma/r$, and the expressions for the volume and surface area of a spherical droplet, $V^l = \sum_i n_i^l v_i = \frac{4}{3}\pi r^3$ and $A = 4\pi r^2$.

Using the incompressible fluid approximation $\mu_i^l(p^l, T) = \mu_i^l(p^v, T) + v_i(p^l - p^v)$ in which $v_i$ is the partial molecular volume of species $i$, one arrives at the so–called Gibbs-Thomson or Kelvin equations:

$$\Delta^*\mu_i + \frac{2\sigma v_i}{r} = 0. \tag{8}$$

In this equation $\Delta^*\mu_i = \mu_i^l(p^v, T) - \mu_i^v(p^v, T)$.

As stated by Wilemski[9], all variables in these equations are functions of bulk composition only. Therefore, at the saddlepoint only the bulk composition can be obtained from these equations. The method described by Laaksonen et al.[17] to calculate $n_i^s$ and $n_i^l$ can not be applied here because the surface molecules do not contribute to the droplet volume in this model. The free energy of formation of a critical cluster at the saddlepoint follows from Eq. (3), with $\Delta\mu_i = 0$, because the critical cluster is in unstable equilibrium with the surrounding vapor:

$$\Delta G_{sp} = \frac{1}{3}\sigma A. \tag{9}$$

## 2.2 Kinetics

The kinetic prefactor $K$ of Eq. (1) was first derived by Reiss[4] and later modified by Stauffer[5]. The result obtained by Stauffer is given by the following equations:

$$K = NR_{av}Z, \tag{10}$$

where $K$ is the product of the number density $N$ of monomers in the gas, an average growth rate $R_{av}$ and the Zeldovich factor Z. $R_{av}$ is given by

$$R_{av} = \frac{\det(\mathbf{R})}{(R_{11}\sin^2\phi + R_{22}\cos^2\phi - 2R_{12}\sin\phi\cos\phi)}, \tag{11}$$

$R_{av}$ depends on the growth rate tensor $\mathbf{R}$ and on the angle $\phi$ of the direction of the current of clusters in the saddlepoint. We shall assume that no cluster–cluster interactions take place, but only monomers collide with the critical cluster, then the elements of $\mathbf{R}$ are given by[5]:

$$\mathbf{R} = \begin{pmatrix} R_{11} & R_{12} \\ R_{21} & R_{22} \end{pmatrix}$$

$$\begin{aligned} R_{11} &= A(n_1, n_2)\beta_1 \\ R_{12} &= R_{21} = 0 \\ R_{22} &= A(n_1, n_2)\beta_2, \end{aligned} \tag{12}$$

where $A(n_1, n_2)$ is the cluster surface area, and $\beta_1$ and $\beta_2$ are the impingement rates of molecules of substances 1 and 2. The expression for the Zeldovich factor is:

$$Z = -\frac{1}{2}\frac{\partial^2 \Delta G(x,y)}{\partial x^2} / (-\det \mathbf{D})^{1/2}. \tag{13}$$

The tensor $\mathbf{D}$ consists of the derivatives of $\Delta G$ with respect to the total number of molecules in the cluster. In combination with CNT, a problem arises in the calculation of $R_{av}$ and $Z$, because $\Delta G$ is not known as a function of the overall cluster composition, but only as a function of bulk composition. Therefore $\mathbf{D}$ can not be determined exactly from this model. However, as already remarked by Wilemski[9], this will not play a crucial role since the influence of $\mathbf{D}$ is limited to the relatively unimportant kinetic prefactor.

# 3 A real gas model for $\Delta G$

Calculation of the nucleation rate according to CNT, requires a thermodynamic description for the gas and liquid mixture taking into account all real gas effects involved in the nucleation process.

First, the bulk composition of the critical droplet can be found by solving an equation that follows from a linear combination of the Kelvin equations:

$$v_2 \Delta^* \mu_1 - v_1 \Delta^* \mu_2 = 0. \tag{14}$$

For given $p$ and $T$, all quantities in this equation are known functions of droplet bulk composition only, which follow from the equation of state.

Second, it is not possible to evaluate mixture properties from the properties of the pure substances; methane is in a state in which no pure liquid methane can exist. Surface tension, which is a very important parameter determining the height of the energy barrier $\Delta G$ in Eq. (1), will thus be estimated by using an empirical correlation (Parachor method).

From several available equations of state we selected the Redlich-Kwong-Soave (RKS) and the Lee-Kesler-Plöcker (LKP) equations, because they proved to be well applicable to alkanes[18]. The RKS equation is of the cubic type and therefore relatively simple from a calculational point of view. The LKP equation of state is a transcendental one, thus computationally more complex. It is applicable, however, over a wider range of reduced temperatures. To compare both EOS to test their suitability to our application, we calculated the equilibrium molar volume of the liquid as a function of temperature and pressure. This is a very important parameter in our model because of its appearance in the Kelvin equations and in the surface tension correlation. The results obtained were compared with experimental data of Shipman et al.[19]. Although RKS is known for its poor prediction of liquid molar volume, results obtained by RKS when Peneloux' correction[18] was included, turned out to be far better than LKP results in predicting the molar volumes (RKS: less than 0.8 % deviation from experimental data, LKP: up to 6 % deviation). For this reason, the RKS equation of state was used for all thermodynamic calculations throughout this work.

The RKS equation has the following form:

$$p = \frac{RT}{V_{RKS} - a} - \frac{b}{V_{RKS}(V_{RKS} + a)}, \tag{15}$$

where

$$a = \frac{0.08664 RT_c}{p_c}$$

and

$$b = \frac{0.42748 R^2 T_c}{p_c} \left[ 1 + f(\omega) \left( 1 - \sqrt{\frac{T}{T_c}} \right) \right]^2,$$

12

with

$$f(\omega) = 0.48 + 1.574\omega - 0.176\omega^2.$$

In these equations, $R$ is the universal gas constant, $V_{RKS}$ is the molar volume (subscript $m$ is left out to avoid confusion with mixture properties in the remainder of this text), $\omega$ is Pitzer's acentric factor and the subscript $c$ refers to the critical point. For a mixture, $a$ and $b$ are evaluated from the pure component values using the mixing rules

$$a_m = \sum_i y_i a_i,$$

$$b_m = \sum_i \sum_j y_i y_j (b_i b_j)^{1/2}(1 - k_{ij}).$$

The quantities $y_i$ in the above expressions denote the molar fractions of the components, both in the vapor and liquid phases. From now on, however, we will use $x_i$ for the liquid molar fractions. In the last mixing rule, the interaction parameter $k_{ij}$ is introduced. Its value is determined by a fit to experiments[20].

The RKS equation is known to yield too large values for the liquid molar volume $V$. The correction term proposed by Peneloux[18] reads

$$V = V_{RKS} - c, \tag{16}$$

where $V$ is the corrected molar volume and

$$c = 0.40768(0.29441 - Z_{RA})\frac{RT_c}{p_c}.$$

$Z_{RA}$ is the Rackett compressibility factor of the substance under consideration. For a mixture, the correction term is obtained by using the conventional mixing rule

$$c_m = \sum_i x_i c_i.$$

From the above equations, an expression for the chemical potential can be derived in analytical form in a standard way by integration of pressure with respect to volume (obtaining the free energy $F$ as a result) and then taking the derivative with respect to $n_i$. In this way an expression of the form $\mu = f(T, V, y_i)$ is obtained. For the liquid, of course, $y_i$ is replaced by $x_i$.

The partial molecular volumes are found by substituting the mixing rules into the RKS equation and applying standard expressions from thermodynamics for the partial volumes ($N_A$ denotes Avogadro's number):

$$N_A v_1 = V_{RKS} - x_2 \frac{\partial V_{RKS}}{\partial x_2} - c_1 \tag{17}$$

$$N_A v_2 = V_{RKS} + x_1 \frac{\partial V_{RKS}}{\partial x_2} - c_2. \tag{18}$$

13

In these equations the Peneloux correction has been used. Because of the use of the incompressible fluid approximation in deriving the Kelvin equations (8), the molecular liquid volume has to be calculated at pressure $p_v$ outside the droplet. Using chemical potentials and molecular volumes obtained from Eqs. (15) to (18) in Eq. (14), a solution for the droplet bulk composition is found, and $\Delta^*\mu_i$ and $v_i$ are known.

With this result, it is possible to calculate the droplet radius from either one of the Kelvin equations written in the form

$$r = -\frac{2\sigma v_i}{\Delta^*\mu_i}. \tag{19}$$

The critical free energy barrier, $\Delta G_{sp}$, is now obtained from Eq. (9), provided that the surface tension is known.

Several correlations exist for the surface tension, most of which need the pure component values as their input. Since relevant temperatures are above the critical temperature of methane, these correlations can not be used for the mixture under consideration. A relation that can be used for our purposes is the Macleod-Sugden correlation[18], an expression obtained by the best fit to experiments. It reads

$$\sigma^{1/4} = \sum_i [P_i]\left(\frac{x_i}{V^l} - \frac{y_i}{V^v}\right) \tag{20}$$

in which superscripts $l$ and $v$ refer to liquid and vapor respectively. The parameters $P_i$ are the so-called parachors of the components. Originally, Macleod suggested to calculate these from molecular structures; however, better agreement with experiments can be obtained by empirically fitting the parachor values to measurements. For our calculations, the values obtained by Deam and Maddox[21] are used. We note that the parachor method is a fit on bulk composition. This is consistent with the fact that, as a solution of the Kelvin equations, bulk compositions are obtained which are substituted into Eq. (20) in order to find the surface tension of the droplet. A limitation of this method is the lack of a proper correction for the curvature of the droplet surface which is still subject of discussion in literature[22-24].

What remains to be calculated, is the kinetic prefactor $K$ of expression (1) in which the second derivatives of $\Delta G$ at the saddlepoint position with respect to the total numbers of molecules, $n_1^t$ and $n_2^t$ are present. As was already pointed out in section 2.2, we have no information concerning the excess numbers $n_1^s$ and $n_2^s$. According to Wilemski[9], the best one can do is using Reiss' original expression for $\Delta G$, i.e.

$$\Delta G(n_1^l, n_2^l) = \sum_{i=1,2} n_i^l \Delta^*\mu_i + \sigma A \tag{21}$$

keeping $\sigma$ constant at the value at critical droplet. The shape of the $\Delta G$ surface obtained in this way is approximately correct in the neighborhood of the saddlepoint.

For the impingement rates $\beta_i$ present in the growth rate tensor $\mathbf{R}$ (Eq. (12)), the ideal expression $\beta_i = \rho_i/\sqrt{k_B T/2\pi m_i}$ is used, where $\rho_i$ is the number density of monomers of

14

species $i$ and $m_i$ is the molecule mass. It is expected that the values of $\beta_i$ only have a slight effect on the nucleation rate.

No special attention has been paid to the limiting case to unary nucleation. It may be expected that a small overestimate of the nucleation rate appears, when the position of the saddlepoint is too close to the $n_1$-axis. This might occur in the low pressure limit, in which only a little methane will be dissolved in the droplets. A more extensive treatment of this matter is given by Wilemski[25].

Finally, we introduce a supersaturation $S$, which will be used in presenting results of our calculations:

$$S = \frac{y}{y_{eq}}, \tag{22}$$

where $y$ and $y_{eq}$ are the molar vapor fractions of nonane in the supersaturated state and at equilibrium, respectively. The equilibrium molar fraction is calculated by equating the chemical potentials in the vapor and the liquid for both components at given $p$ and $T$. We emphasize that this definition is *not* used in the calculation of nucleation rates. The reason for using the supersaturation ratio in representing the results is that $S$ is considered to be the driving force behind the condensation process.

The calculations described are implemented in a FORTRAN numerical code. Calculations can be performed for $n$-alkanes (up to $n$-dodecane) with several carrier gases. The numerical values of the mixture methane/$n$-nonane, used in the present calculations, are listed in the appendix. The program code is available upon request.[1]
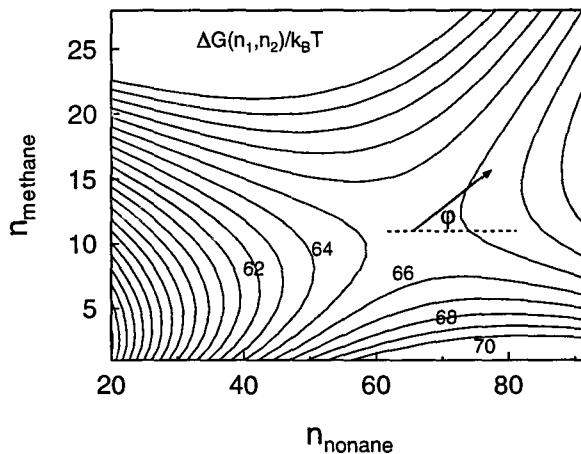


Figure 1: *Contourplot of the free energy surface in the vicinity of the saddlepoint. $T = 240\ K$, $p = 40\ bar$ and $y_1 = 1 \cdot 10^{-4}$ ($S \simeq 8$). Value of $\Delta G$ at the saddlepoint is $65.5\ k_B T$; contours correspond to increment steps of $1\ k_B T$.*

---

[1]For future users, a block scheme of the code is listed in appendix A at the end of this thesis. This scheme is not included in the original text of the article.

# 4 Results and discussion

A plot of a typical free energy surface according to Eq. (21) for the $n$-nonane/methane mixture is shown in Fig. 1. The conditions are: $T = 240$ K, $p = 40$ bar and the molar fraction of $n$-nonane in the gas $y_1 = 1 \cdot 10^{-4}$ corresponding to a saturation ratio $S \approx 8$. The critical cluster consists of 66 nonane molecules and 11 methane molecules. During nucleation, the saddlepoint is crossed in the direction $\phi$ indicated by the arrow.



Figure 2: *Nucleation rate in the mixture methane/$n$-nonane as a function of supersaturation with the total pressure as a parameter. Temperature $T = 240$ K.*

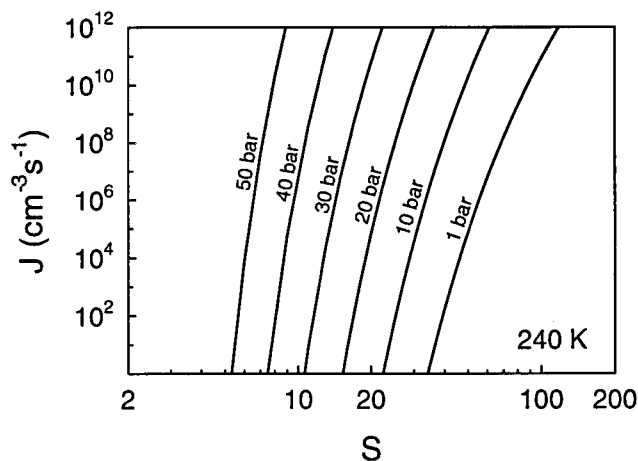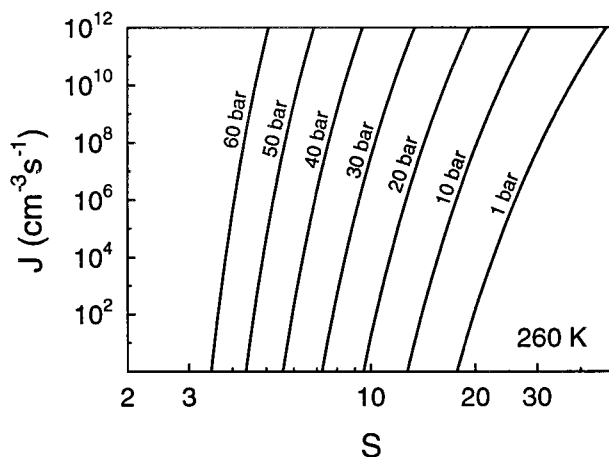

Figure 3: *Nucleation rate in the mixture methane/$n$-nonane as a function of supersaturation with the total pressure as a parameter. Temperature $T = 260$ K.*

Figures 2 and 3 show the nucleation rate as a function of supersaturation with the pressure as a parameter for two different temperatures. The model predicts a large effect of total pressure on the nucleation rate. At fixed supersaturation, increasing pressure

16

induces an increase of nucleation rate by several orders of magnitude demonstrating real gas effects in homogeneous nucleation. Apart from this phenomenon, the generally observed exponential dependence of nucleation rate on supersaturation at given total pressure and temperature can also be seen in the figures.
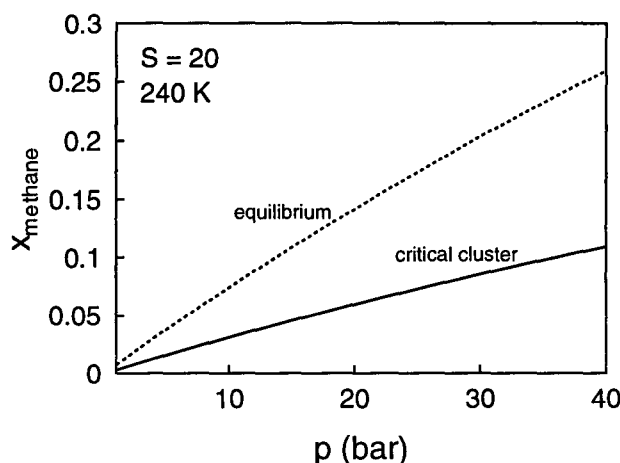


Figure 4: *Methane liquid fraction as a function of total pressure. Solid line represents the composition of the critical droplet at a vapor nonane fraction $y_1 = 1 \cdot 10^{-4}$. Dashed line is equilibrium liquid, temperature $T = 240$ K.*

The interaction of nonane and methane in the nucleation process also comes forward when the composition of the critical cluster is considered. The saddlepoint of Fig. 1 already indicated the presence of methane in the critical cluser. In Fig. 4 the molar fractions of methane in the critical cluster and in the corresponding equilibrium liquid state are plotted as a function of pressure at fixed supersaturation and temperature. The methane molar fraction increases from approximately 0 at low pressure to 0.11 at 40 bar. This is less than the equilibrium molar fraction, but, as can be seen from Fig. 5, it has significant consequence for the surface tension. The increasing amount of methane in the critical cluster lowers the surface tension from $2.7 \cdot 10^{-2}$ N/m to $1.9 \cdot 10^{-2}$ N/m at 40 bar. The decrease of surface tension has a direct consequence for the energy barrier $\Delta G$ (Eq. (9)) which is also reduced. This largely explains the enhanced nucleation rate with pressure.

In figures 2 and 3 the nucleation rate was plotted as a function of supersaturation $S$. It has to be realized here that the saturated nonane vapor density itself depends on the mixture total pressure, as is shown in Fig. 6. Due to real gas effects, the solubility of nonane in the gas phase increases, resulting in an increase of nonane concentration and therefore an even stronger increase of equilibrium nonane vapor density, at pressures above 20 bar. So, $S$ is not a measure for the actual nonane vapor density when nucleation rate curves at different pressures are compared.

In Fig. 7 the nucleation rate is plotted as a function of nonane vapor density $\rho_1$ which is obtained from the relation $\rho_1 = y_1/V^v$, where $V^v$ is the molar volume of the vapor mixture. An increase of total pressure above 10 bar at fixed nonane vapor density and
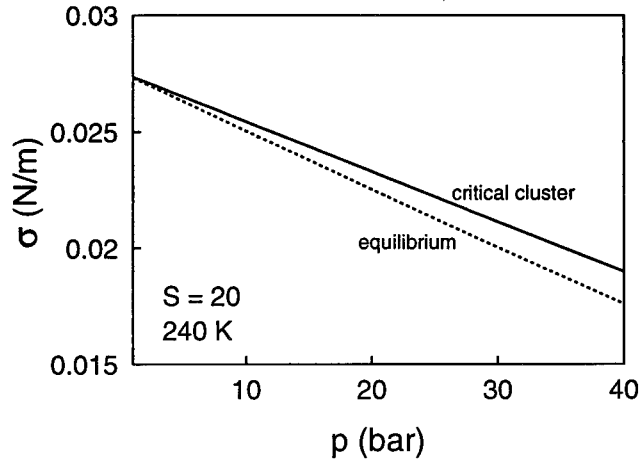
Figure 5: *Surface tension as a function of pressure. Solid line represents critical droplet composition at a vapor nonane fraction $y_1 = 1 \cdot 10^{-4}$. Dashed line is equilibrium liquid, temperature $T = 240$ K.*



Figure 6: *Pressure dependence of the equilibrium gas composition of the mixture methane/-n-nonane. The dashed curve gives the nonane molar fraction in the gas phase at vapor–liquid equilibrium at 240 K as a function of the mixture total pressure. The solid curve gives the corresponding equilibrium nonane vapor density.*

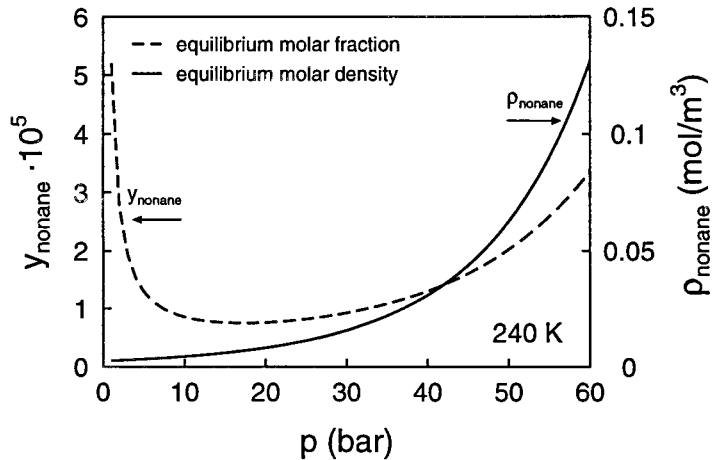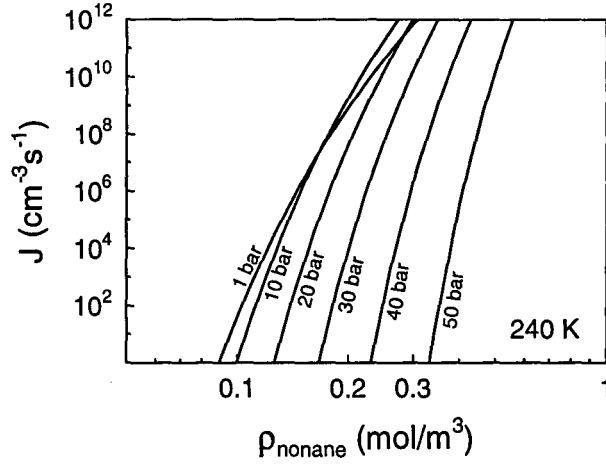Figure 7: *Nucleation rate in the mixture methane/n-nonane as a function of nonane vapor density for different total pressures at a temperature $T = 240\ K$.*

temperature apprears to reduce the nucleation rate. This can also be observed in Fig. 8. In this plot the nucleation rate is given as a function of pressure (solid curve) with a fixed nonane vapor density of $\rho_1 = 0.25$ mol.m$^{-3}$. The dashed curve shows the nucleation rate if not methane, but an inert carrier gas is added. The pronounced difference between
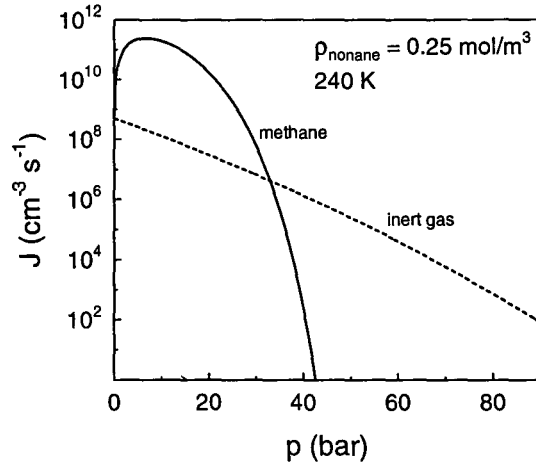


Figure 8: *Nucleation rate as a function of pressure for a fixed nonane density $\rho_1 = 0.25$ mol.m$^{-3}$. The solid curve indicates values for the methane/n-nonane mixture, calculated with binary theory. The dashed line indicates the values of CNT for n-nonane with an inert carrier gas. Temperature $T = 240\ K$.*

binary nucleation under real gas conditions and unary nucleation with an inert carrier gas is clear. Adding methane to nonane first shows a strong increase of nucleation rate, due to the lowering of surface tension caused by the presence of methane in the critical cluster. So, initially this effect dominates the effect of decreasing supersaturation with pressure. At higher pressures, the situation is reversed and finally, when pressure is high

19

enough, thermodynamic equilibrium is attained again. Adding an inert component to a nonane vapor of fixed density shows a monotonically decreasing nucleation rate with (inert) gas pressure, this being a result of a higher energy barrier due to the increase of liquid chemical potential, while vapor chemical potential is not changed much. Recently, a reduction of the nucleation rate with increasing total pressure of 1–propanol in helium and in hydrogen, was experimentally found by Heist et al.[26] in a special high pressure diffusion cloud chamber.
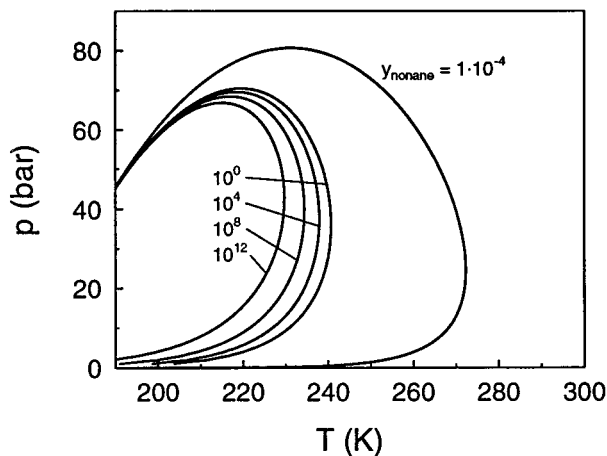


Figure 9: $p - T$ diagram with lines of constant nucleation rate for a mixture of $1 \cdot 10^{-4}$ molar fraction n-nonane. The outer curve corresponds to vapor–liquid equilibrium for given nonane fraction. The labels denote the nucleation rate in $cm^{-3}s^{-1}$.

Finally, in Fig. 9 a $p - T$ phase diagram is showed of a methane/$n$-nonane mixture with a nonane molar fraction of $1 \cdot 10^{-4}$. The outer curve, on which the gas mixture with given nonane concentration is in equilibrium with the liquid phase, forms the boundary of the two–phase coexistence region. Inside this envelope, lines of constant nucleation rate are drawn, lines representing higher nucleation rates are found further inwards the coexistence region. Furthermore, lines of given nucleation rate form "retrograde curves", and they all appear to converge to the critical point of the mixture.

# 5 Conclusions

The classical binary nucleation theory has been extended with a thermodynamic model taking into account real gas effects. For calculating chemical potential and molar volumes the RKS equation of state was applied, surface tension was modeled with the Parachor method. This model enables the theoretical study of homogeneous nucleation of real gas mixtures in the coexistence region, such as the methane/$n$-nonane mixture, subject of the calculations performed in this paper. The model predicts for this mixture an increase of nucleation rate with pressure when supersaturation and temperature are fixed. Due to real gas effects, an increasing amount of methane is present in the critical

droplet with increasing pressure, as also occurs in equilibrium condensation. The presence of methane in the critical cluster lowers the surface tension, and therefore the free energy of formation is lowered, leading to an enhanced nucleation rate.

We have only presented calculations for the methane/$n$-nonane mixture. However, it is to be expected that similar results are found in other mixtures at high pressures, when interactions between the mixture components are present. An example is the nitrogen/$n$-nonane mixture.

Up to now no experimental data of homogeneous nucleation in the coexistence region at high pressures have been published in literature. Experimental work with a nucleation pulse expansion wave tube is in progress[27,28]. Results will be published separately.

# Appendix

Numerical values of the methane/$n$-nonane mixture used in the calculations are listed below.

*n-Nonane:* critical pressure $p_c = 22.9$ bar, critical temperature $T_c = 594.6$ K, Pitzer's acentric factor $\omega = 0.445$, Racket compressibility factor $Z_{RA} = 0.2543$, Molecular mass $m = 128.259$ g/mol, and Parachor $P = 387.6$ kg$^{1/4}$m$^3$s$^{-1/2}$mol$^{-1}$.

*Methane:* critical pressure $p_c = 46.0$ bar, critical temperature $T_c = 190.4$ K, Pitzer's acentric factor $\omega = 0.011$, Racket compressibility factor $Z_{RA} = 0.2892$, Molecular mass $m = 16.043$ g/mol, and Parachor $P = 81.0$ kg$^{1/4}$m$^3$s$^{-1/2}$mol$^{-1}$.

The interaction parameter for the mixture $k_{ij} = 0.0448$. All listed data can be found in the book of Reid, Prausnitz, and Poling[18], except for the binary interaction parameter which comes from Knapp *et al.*[20].

# References

[1]M.J.E.H. Muitjens, V.I. Kalikmanov, M.E.H. v. Dongen, and A. Hirschberg, Revue de l'institute Français du pétrole **47**, 63 (1994).

[2]M. Volmer and A. Weber, Z. Phys. Chem. **119**, 277 (1926).

[3]R. Becker and W. Döring, Ann. Phys. **5**, 719 (1935).

[4]H. Reiss, J. Chem. Phys. **18**, 840 (1950).

[5]D. Stauffer, J. Aerosol Sci. **7**, 319 (1976).

[6]R.G. Renninger, F.C. Hiller, and R.C. Bone, J. Chem. Phys. **75**, 1584 (1981).

[7]G.J. Doyle, J. Chem. Phys. **75**, 1585 (1981).

[8]G. Wilemski, J. Chem. Phys. **80**, 1370 (1984).

[9]G. Wilemski, J. Phys. Chem. **91**, 2492 (1987).

[10]G. Wilemski, J. Chem. Phys. **88**, 5134 (1988).

[11]J.W. Gibbs, *The scientific papers of J.W. Gibbs volume 1*, (Dover, New York, 1961).

[12]J.S. Rowlinson and B. Widom, *Molecular theory of capillarity*, (Clarendon Press, Oxford, 1982).

[13] J. Lothe and G.M. Pound, J. Chem. Phys. **36**, 2080 (1962).

[14] A. Dillmann and G.E.A. Meier, J. Chem. Phys. **94**, 3872 (1991).

[15] X.C. Zeng and D.W. Oxtoby, J. Chem. Phys. **95**, 5940 (1991).

[16] H.R. Kobraei and B.R. Anderson, J. Chem. Phys. **94**, 590 (1991).

[17] A. Laaksonen, M. Kulmala, and P. E. Wagner, J. Chem. Phys. **99**, 6832 (1993).

[18] R.C. Reid, J.M. Prausnitz, and B.E. Poling, *The Properties of Gases and Liquids*, (McGraw-Hill Book Company, New York, 1987).

[19] L.M. Shipman and J.P. Kohn, J. Chem. Eng. Data **11**, 176 (1966).

[20] H. Knapp, R. Döring, L. Oellrich, U. Plöcker, and J.M. Prausnitz, *Vapor-Liquid Equilibria for Mixtures of Low Boiling Substances*, (Deutsche Gesellschaft für Chemisches Apparatewesen, Frankfurt am Main, 1982).

[21] J.R. Deam and R.N. Maddox, J. Chem. Eng. Data **15**, 216 (1970).

[22] R.C. Tolman, J. Chem. Phys. **17**, 333 (1949).

[23] S.M. Thompson, K.E. Gubbins, J.P.R.B. Walton, R.A.R. Chantry, and J.S. Rowlinson, J. Chem. Phys. **81**, 530 (1984).

[24] M. Nijmeijer, C. Bruin, A.B. van Woerkom, A.F. Bakker, and J.M.J. van Leeuwen, J. Chem. Phys. **96**, 565 (1992).

[25] G. Wilemski, J. Chem. Phys. **62**, 3763 (1975).

[26] R.H. Heist, M. Janjua, and J. Ahmed, J. Phys Chem. **98**, 4443 (1994).

[27] K.N.H. Looijmans, P.C. Kriesels, and M.E.H. Van Dongen, Exp. Fluids **15**, 61 (1993).

[28] K.N.H. Looijmans, J.F.H. Willems, and M.E.H. v. Dongen, in *Proceedings of the 19th Int. Symp. on Shock Waves*, Springer Verlag, to be published.

# Chapter 3

# Condensation experiments

## 3.1 Introduction

As already remarked in chapter 1, a fast expansion is an excellent means to create a supersaturated state. "Fast" here means that the expansion can in good approximation be considered isentropic, so that the temperature decreases together with pressure. Since the equilibrium density of a vapour depends strongly on temperature, a supersaturated state can be reached during the expansion.

One way to achieve a controllable and fast expansion is to make use of the expansion wave that travels in the opposite direction of the shock wave in a shock tube. The temperature after the expansion can be controlled by varying the pressure ratio between the high pressure section (HPS) and low pressure section (LPS) of the tube; when the molar fraction of nonane is known (which is not assumed to change during the expansion), the value of the supersaturation ratio $S$ after the expansion is also a known quantity.

By introducing a small local widening in the low pressure section of the tube, even a pulse-like variation of $S$ can be obtained. This principle will be described in section 3.2. Since nucleation rates depend very strongly on supersaturation – which will be obvious from the previous chapter – the only significant nucleation will take place during the pulse. After the pulse, however, $S$ still exceeds unity, so that the nuclei formed will grow to macroscopic sizes and can be optically detected. The optical detection will be the subject of section 3.3. In this way information is obtained on the nucleation rate by simply "counting" the droplets per unit volume and dividing by the duration of the nucleation pulse. Because the pulse duration is very short, the droplets formed all have approximately the same sizes. This has the advantage that information can be obtained on the droplet radius as a function of time, which is the growth rate.

In addition to the nucleation and droplet growth rates, the thermodynamic state at which these quantities are measured is important. The state of a binary mixture of gases is characterized by the temperature $T$, the pressure $p$ and the molar vapour fraction $y_v$. The determination of $p$ and $T$ will be the subject of section 3.4, together with the time duration of the nucleation pulse.

For the determination of the composition of the mixture, a choice can be made out of several methods. A technique based on selective adsorption and gas chromatography is recently being used within our group. This method and the others, together with their pro's and cons, will be described in section 3.5.

In section 3.6 the experimental procedure of a nucleation experiment will be described in some detail.

## 3.2 Experimental setup

A schematic representation of the nucleation pulse shock tube can be seen in figure 3.1. It is a modification of the expansion-shock tube developed by Peters [1].

At time zero, the membrane is heated by a hot ribbon and opens within approximately
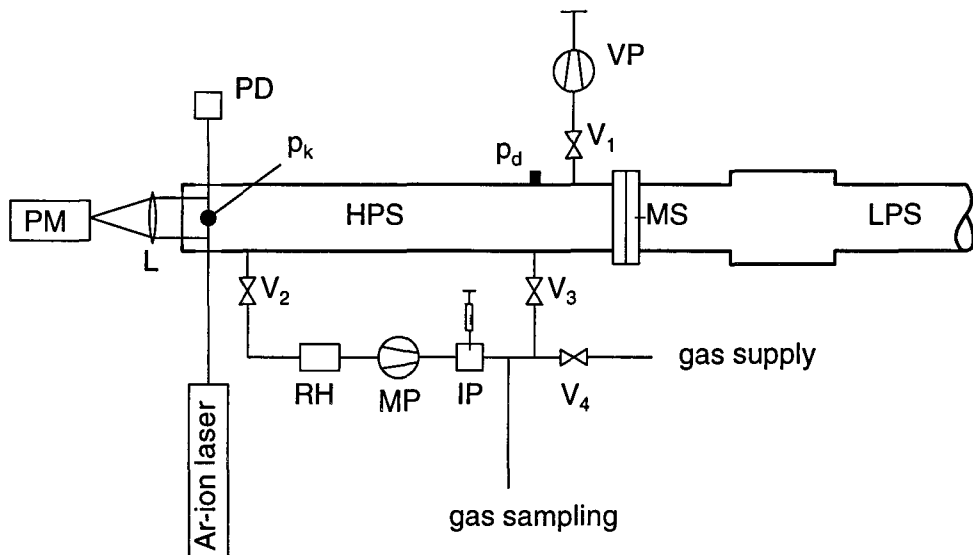


| HPS | high pressure section | $V_{1,...,4}$ | valves |
|-----|----------------------|--------------|--------|
| LPS | low pressure section | VP | vacuum pump |
| MS | membrane section | MP | mixing pump |
| PM | photomultiplier | IP | injection point |
| PD | photodiode | $p_d$ | static pressure (Druck PDCR 200) |
| L | lens | $p_k$ | dyn. pressure (Kistler 603 B) |
| RH | humicap | | |

Figure 3.1: *Schematic representation of the nucleation pulse shock tube setup.*

100 $\mu$s [2]. A shock wave travels into the LPS; an expansion wave travels in opposite direction. The shock wave reflects at the local widening as another small expansion, followed by a small recompression as it reaches the end of the widening. In figure 3.2 a simulation of the propagating waves is represented in a $(x, T)$-diagram. The numerical method used is the one-dimensional Random Choice Method (RCM); details of this method can be found in references [2, 3, 4]. For convenience, a schematic drawing of

24

the tube and the development of the pressure at the HPS endwall are also included in the figure.
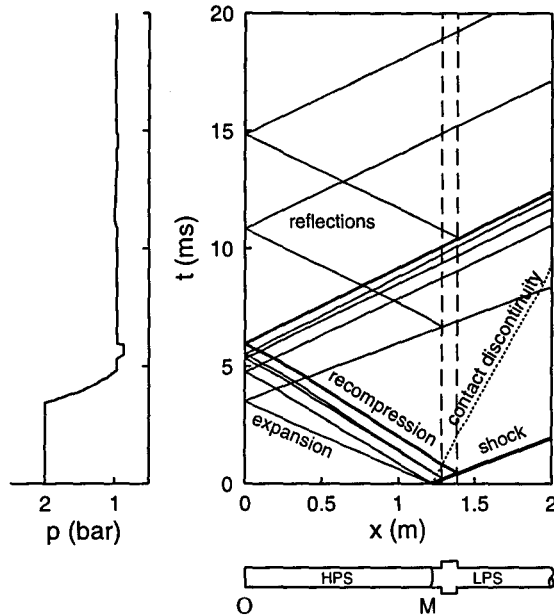


Figure 3.2: $(x,T)$-diagram of the wave propagation in the expansion shock tube.

The pressure dip due to the local widening – which is in fact the nucleation pulse – is typically 0.4 ms in time. This can be varied by mounting a widening of different length into the tube. After typically 30 ms, the shock wave – that has reflected at the LPS endwall in the meantime – arrives at the HPS endwall and brings the experiment to an end. The gasdynamic aspects of the setup are described in more detail by Looijmans *et al.* [2].

## 3.3  Droplet concentrations and growth

For the determination of the droplet concentration in the mixture during the experiment, use is made of an optical setup (see figure 3.3).

A laser beam is sent through the HPS in transversal direction at about 5 mm from the endwall. In this way the velocity of the gas at the point of detection can be neglected during the experiment, whereas detection still takes place outside the thermal boundary layer at the endwall.

The transmitted beam is sent through a thick glass plate, whereby the first outcoming reflection is measured (this means a reduction of intensity with respect to the primary beam by a factor of about 600). The intensity of this beam is recorded with a photodiode.

While doing experiments at low pressures with the expansion shock tube, the transmitted beam was lead through a circular diaphragm to reduce the influence of forward
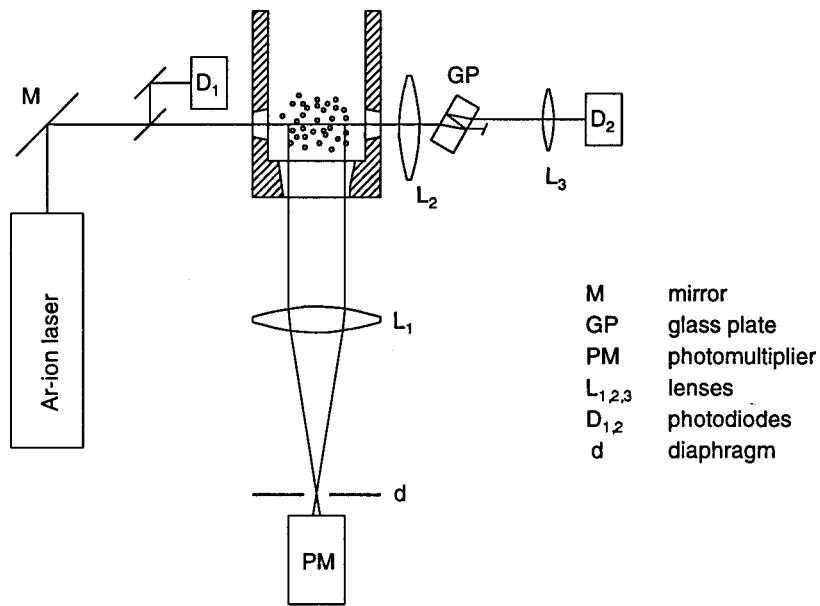
25

Figure 3.3: *Optical setup for determining concentration and radius of the droplets formed.*

scattered light on the signal. At high pressures the refraction index of the gas mixture starts differing significantly from unity. This, in combination with the oblique placement of the tube windows, causes the transmitted beam to deviate from its original propagation direction. In the stationary initial state this can easily be corrected for by moving the photodiode $D_2$. During the expansion, however, the refraction index decreases again and the transmitted beam again changes its propagation angle. The described effect is so large that the diaphragm can not be used with the high pressure experiments any more, and has to be replaced by lens $L_3$ to make sure that the beam keeps falling on photodiode $D_2$. Consequently, there is also some forward scattered light included in the transmission signal. Calculations show that the contribution of this forward scattered light to the transmitted signal can be as large as 10% using lens $L_3$. Since the beam deviation is only in vertical direction, $L_3$ could be combined with a slit-shaped diaphragm to reduce the influence of forward scattered light.

When droplets are formed, the transmitted beam is attenuated. The droplet concentration can be derived from the amount of attenuation according to the Lambert-Beer law.

For very low droplet concentrations, a problem arises with this method in view of the very high experimental pressures: some disturbances due to the propagation of the shock wave in the tube are inevitable. In combination with the small attenuation at low concentrations, this causes the signal-to-noise ratio to fall to a value that cannot be used for a proper determination of the transmission coefficient anymore. The solution to this problem will be given later in this section.

The size of the droplets as a function of time is obtained by recording the intensity of the light scattered within a small solid angle of the direction perpendicular to the incident beam (90°-scattering). For particles with sizes of the order of the wavelength of light (hundreds of nanometers), the Mie theory describes the intensity scattered by spherical particles as a function of scattering angle, index of refraction $n$ and dimensionless radius $2\pi r/\lambda$ ($\lambda$ being the wavelength of the incident light). Details of this theory can be found in references [5, 6]. A typical Mie pattern is plotted in figure 3.4.
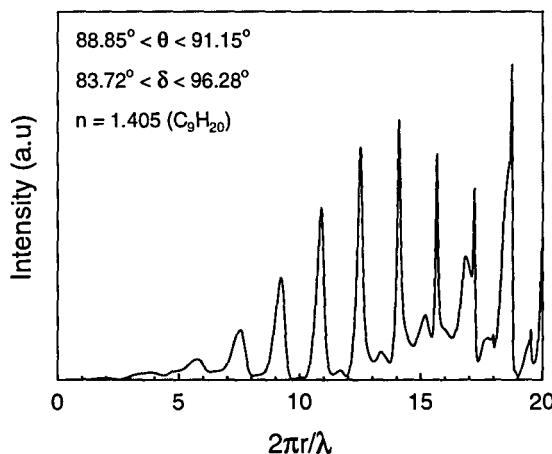


Figure 3.4: *Typical Mie pattern of the intensity scattered by spherical droplets versus dimensionless radius $2\pi r/\lambda$. Scattering angle is 90°, index of refraction is 1.405.*

In our optical setup, the recorded intensity of the scattered light has – to a very high degree of accuracy – the same form, but now as a function of time. Measured peaks can be identified with the theoretical ones and so, knowing the wavelength and index of refraction, the droplet radius can be obtained as a function of time very accurately. In principle, this can be done for $r$ being a continuous function of time; it is sufficient, however, only to consider the peak tops in order to determine the growth rate.

Here, a remark has to be made about the detection limits of the scattering setup. The lower limit is constituted by the recognizability of the peaks (thus by the signal-to-noise ratio). The upper limit is formed by the saturation limit of the measuring device (photomultiplier + acquisition system). Consequently, the measurable droplet concentrations are all within a range of about a factor $10^4$ (nucleation rates have been measured varying from $4 \cdot 10^{13}$ m$^{-3}$s$^{-1}$ up to $3 \cdot 10^{18}$ m$^{-3}$s$^{-1}$).

Now, the procedure during a series of experiments is as follows. One experiment of the series, the one with the highest measurable droplet concentration, is chosen as the reference experiment. The droplet concentration is derived from the transmitted light attenuation. Other experiments, all with lower concentrations, are related to the

reference experiment by comparison of absolute heights of corresponding Mie-peaks. The ratio of the intensity of the highest detectable peak to that of the reference peak is taken and multiplied by the droplet concentration in the reference experiment. After a correction due to the intensity of the incident beam, which differs slightly from one experiment to another, the droplet concentration is obtained for the other experiments, even if they are below the detection limit of the attenuation method.

## 3.4  Thermodynamic state and pulse duration

A thermodynamic variable that is relatively easy to measure is obviously the pressure $p$. Making the assumption that the expansion is isentropic, the temperature $T$ is calculated from the standard isentropic gas relations, whereby real gas effects are taken into account with the aid of the RKS equation of state described in chapter 2. Details of this calculations can be found in [7].

In this manner, $p$ and $T$ are known as continuous functions of time. The pressure and temperature during the nucleation pulse are known then; it's these values that come into the relationship $J(p, T, y_v)$ that is going to be determined.

Some effort has been made to validate the isentropicity assumption by measuring temperature directly, making use of hot wires. This turned out to be extremely difficult for mainly two reasons.

First, there are two competitive factors. The time constant $\tau$ of the hot wire setup is enlarged (with respect to the conventional use as a velocity measuring device) by the fact that gas velocities at the endwall are very low during the experiment. Heat transfer can only take place by conduction through the gas and is therefore very slow. Consequently, the wire certainly has to be as thin as possible in order to be able to follow the temperature changes on a millisecond scale. However, at the end of the experiment, the shock wave reaches the endwall and exerts a force on the wire. For this reason the wire has to be strong and thus either thick (which is in contradiction with the above argument) or very short.

But then the second complicating factor appears, which is the influence of the end supports of the wire. They have to be electrically conducting (the measurement is based on the temperature dependence of the wire's resistance), so they will also be good thermal conductors. Therefore, they will remain at wall temperature, which keeps the wire from fully attaining the gas temperature. In this way the temperature can not be measured with the desired accuracy of $\pm 1$ K. A method based on coated hot wires has been studied but not yet carried out.

In practice the bottom of the pressure dip is not exactly flat. In other words: the thermodynamic state changes during the pulse. The change is only slight, but slight changes in state can cause huge changes of nucleation rates (a temperature increase of 1 K can cause $J$ to decrease by a factor 10 to 100!). For the experimental value of $J$

this constitutes no problem, for $J$ is measured with a reasonable accuracy (within 20%, see section 4.5), but the complicating factor is the uncertainty in $T$ when comparing experimental results to theoretical predictions: what precise values of $p$ and $T$ should be inserted into the theory?

To get around this problem and simultaneously obtain the time duration of the nucleation pulse, the following procedure is used. Two points are identified as the beginning and end of the pressure dip. These points are the first and the last point with pressures representative for the average value over the dip. The time interval between these points is taken to be the pulse duration. Further, the average pressure (and corresponding temperature) over the two chosen points is taken to be the condensation pressure (resp. temperature).

A disadvantage of the described method is, that there can be some ambiguity in the results: sometimes the pressure pulse has rather vague borders, so that not every experimentator will choose the same points. Therefore, an extra uncertainty is introduced into both the pulse duration and in the thermodynamic state that is identified as the nucleation state. This problem can be solved by integration over the pulse based on classical theory and empirical data. This method will be described in appendix B.

## 3.5   Composition of the mixture

The composition of the mixture is up to now the most difficult quantity to measure accurately. Three methods will be described here, the first of which is the most widely used but has to be abandoned already at moderate pressures (above a few bars). It is still subject of discussion which one of the other two methods applies best.

The most generally used method is the following. The molar density of the vapour is calculated from the initial vapour pressure with the ideal gas law and is assumed not to change when the other component (the gas) is added. The total molar density is calculated from the total pressure of the mixture with a real gas equation of state. The vapour fraction is now equal to the ratio of the two densities.

The shortcoming of the method lies in the above assumption that the vapour density does not change upon addition of the gas. When the vapour is injected, the vapour pressure indicates that not all the nonane has vaporized: some nonane is adsorbed at the tube walls in the liquid phase. Upon addition of the gas the chemical potential of the liquid is raised, whereas the chemical potential of the vapour changes only slightly. It is thus likely that more nonane dissolves into the gas phase. This can in no possible way be taken into account by this method.

The second method is based on selective adsorption and gas chromatography. A column filled with an adsorbens is mounted onto the mixing circuit of the shock tube (see figure 3.5). After the mixing of nonane and methane, so immediately before the experiment, a sample of the mixture is lead through the column. The nonane attaches to the

adsorbens, whereas the methane passes through. The volume of the passing methane is measured with a glass cilinder placed upside down in a water reservoir; when a few hundreds of milliliters have passed, the valve $V_1$ is closed.
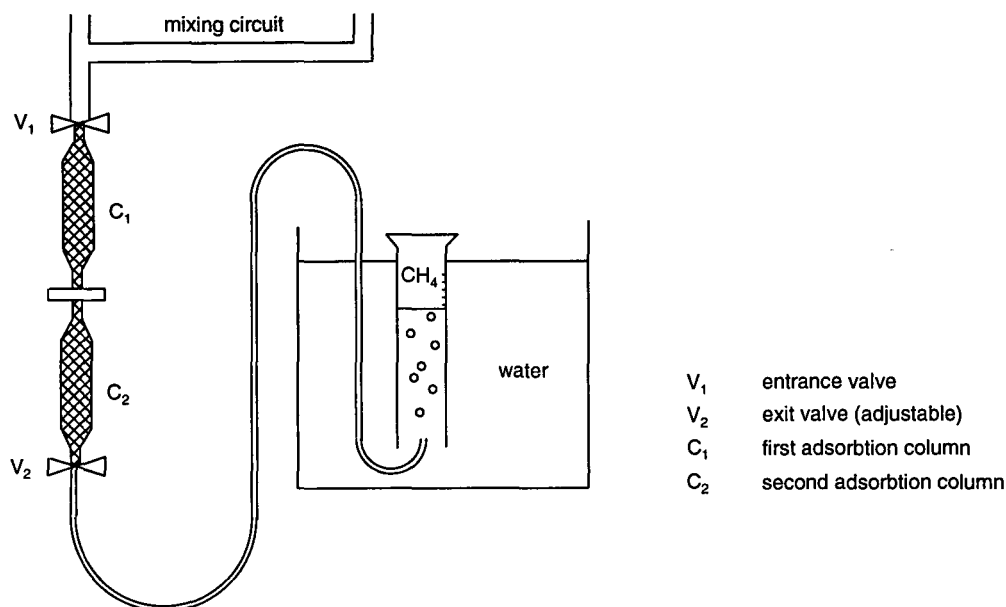


Figure 3.5: *Schematic representation of the gas sampling setup.*

After the experiment, the column is taken off the circuit and flushed with hexane. The nonane dissolves into the hexane, yielding a known volume of nonane solution. The column is flushed two times to make sure that all the nonane has dissolved. Both samples are injected into a gas chromatographer to determine the nonane concentration; hence, the absolute amount of nonane in the original sample is known and thus the molar fraction.

During the first series of experiments there were two columns in a row in order to test the effectivity of the adsorbens. The second column in all cases turned out to contain a negligible amount of nonane.

The gas sampling technique has only recently been used in our group for analysis of high pressure gas mixtures. The accuracy of the method was originally estimated to be ±5%; the uncertainty could be somewhat greater, however, according to recent experiments by M. Verschueren [8]. The reason lies in the beginning of the sampling: when the valve $V_1$ is opened, the gas mixture — with a pressure of typically tens of bars — expands into the column of atmospheric pressure. This could cause some preliminary condensation, so that a liquid reservoir is formed at the entrance valve. This influences both the nonane content of the sample to be taken *and* that of the following samples because of the resident liquid reservoir. The solution to this problem is being sought in bringing the sampling column to a higher pressure, nearly as high as that of the mixture, before the experiment. Testing of this procedure is still in progress.

The last method that is used to determine the nonane molar fraction is based on the droplet growth stage. As already mentioned, the growth rate can be measured very accurately with the shock tube setup. A numerical code for the calculation of binary droplet growth, based on Gyarmathy's growth model, has been developed some time ago by van Beeck [9, 10]. Details of the growth model can be found in his work.

The nonane molar fraction is one of the input parameters to calculate the growth rate. By adjusting it until the growth rate is in agreement with the experiment, a value of the molar fraction can be obtained.

Of course, the validity of this method depends on the correctness of the growth model at high pressures. This should be subjected to a close examination, for it is in fact the easiest way to obtain the molar fraction. Once the growth model has proven to be correct, the fraction can be obtained without any experimental effort.


## 3.6 Experimental procedure

In this section, the procedure that is followed during a high pressure nucleation experiment is outlined.

After mounting a new membrane, an experiment starts with the evacuation of the tube. The LPS is evacuated until the pressure is lower than 1 Pa; the HPS is brought below $10^{-3}$ Pa and then pumping is continued during 60 minutes.

After that, the leakage rate is determined during 30 minutes. In fact, this is a combination of both gas leakage through small openings (the most important leak factor being the membrane chamber) and of vapour coming off the tube walls. A typical value of this total leakage rate is 0.1 Pa/min. The "pure" leakage rate (not taking into account the gas coming off the walls) can be determined by leaving the system vacuum for some days and then measuring the leakage rate. Typical values for this leakage rate are about 0.04 Pa/min.

Once again the HPS is evacuated, but now pumping is continued only during 5 minutes.

Then liquid nonane is injected. The injection volume depends on the desired saturation ratio during the experiment, but a simple relationship between injection volume and saturation before or after the expansion can not be given because of the strong nonlinear behaviour of the initial vapour pressure with injection volume. In fact, the injection volume is at first determined by a trial-and-error procedure: once a good experiment has been done, the rest of the series of experiments is carried out by slightly varying the injection volume of the successful experiment. After injection the pressure rises to typically 300 Pa, but lowers during about ten minutes by a few percents. After half an hour the pressure has stabilized. The value it has attained then – corrected for the pure leakage – is recorded as the initial vapour pressure. The pressure transducer used for this goal is a Barocel type 600A.

Immediately after that, the gas (in this work methane or argon) is added. Simultaneously, the LPS is brought to its desired initial pressure. This has to do with the

choice of the membrane: it must be thick enough to hold the initial pressure difference between HPS and LPS, but on the other hand it must be thin enough to open easily when heated by the hot ribbon. In view of the fact that membrane burst pressures (thicknesses) are chosen so critically, the LPS is always kept under the HPS pressure to prevent the membrane from bowing back and forth (this could cause an undesired early bursting).

When the pressure in the HPS has reached its desired value, the mixing pump is put on. Pumping is continued during a quarter of an hour. This duration is not arbitrary. In the mixing circuit it is possible to monitor the relative humidity of the mixture passing by means of a Humicap HMP 124B hygrometer, see figure 3.1. While doing experiments with water under high pressures, it was noticed that the signal of the Humicap showed an oscillation when the mixing pump was turned on; the oscillation in all cases damped out to a constant value (i.e., constant humidity) within a quarter of an hour. This means that it takes at most this time to homogenize the mixture. It is assumed that this does not depend on the components of the mixture.

While the mixing pump is working, the laser beam is put on to give it some time to stabilize before the experiment starts.

After mixing, a sample of the gas is taken and then the mixing circuit is closed. Leaving it open would cause disturbances of the wave propagation behaviour of the tube described in section 3.2.

Now everything is ready for the experiment. Initial HPS and LPS pressures and initial temperature are recorded. The dynamic pressure transducer (Kistler type 603 B, in combination with a Kistler type 5001 charge amplifier) is put in its operating state. This is done just now to prevent its output signal from drifting. Then a pulse current is sent through the heating ribbon in the membrane chamber, the membrane bursts and the experiment starts.

During the experiment four signals are recorded: the dynamic pressure, the intensity of the reference beam and the transmitted beam (both by means of a photodiode) and the intensity of the light scattered under 90°, see section 3.3. These signals are recorded with a sampling rate of 32 kHz into a LeCroy 6810 waveform recorder, which is triggered by the dynamic pressure signal falling below a threshold value. Typical results are described in the next chapter.

# Chapter 4

# Experimental results

## 4.1 Introduction

This chapter deals with the results of the high pressure nucleation experiments. To get a more concrete idea of this kind of experiments, a typical example is described in section 4.2.

Results on the $n$-nonane/methane mixture are given in section 4.3, followed by the results on $n$-nonane/argon in section 4.4. A qualitative comparison to the model described in chapter 2 will also be included in these sections.

Since high pressure experiments with the expansion shock tube have only recently become possible, it is important to know what experimental errors are involved, and what their influence on the interpretation of experimental results is. This is the subject of section 4.5.

## 4.2 A typical high pressure experiment

In this section typical results of a high pressure nucleation experiment are described.
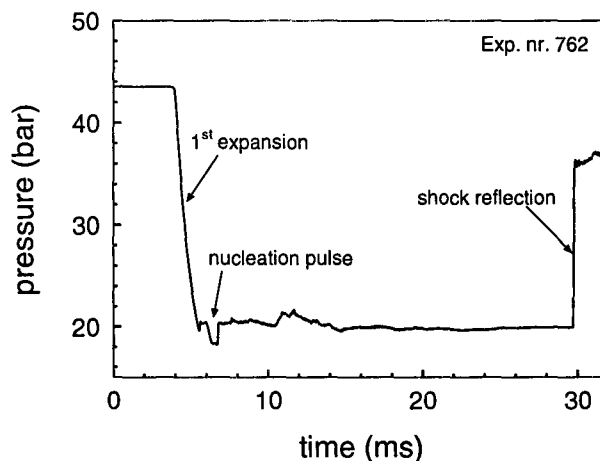
Figure 4.1: *Typical pressure history at the endwall of the high pressure section.*

The pressure history at the endwall of the HPS is shown in figure 4.1 for an experiment

with an initial pressure of 43.7 bar and a condensation pressure of 18.8 bar. As far as the dynamic pressure is concerned, no special differences – apart from the faster propagation of the waves – can be observed in comparison to low pressure experiments, which have been performed earlier by Van Schaijk [11] in order to test the measuring technique. For the two other signals, however, there are some important differences.

The transmitted light curve is less smooth than in comparable low pressure experiments. The transmission signal for the example experiment can be seen in figure 4.2.
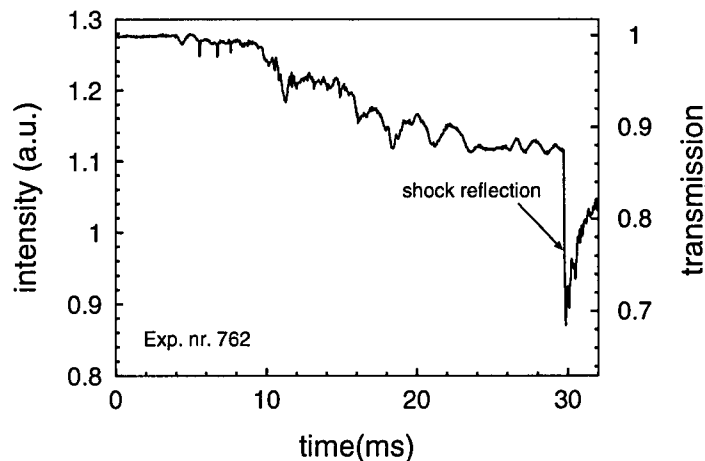


Figure 4.2: *Transmission signal for the example experiment.*

During the experiment (from $t = 4$ ms to $t = 30$ ms), the signal shows some disturbances that might be due to tube resonances caused by the propagation of the waves in the tube. Since the reference experiment of a series is always chosen to be the one with the highest signal-to-noise ratio[1] and therefore the smallest relative error (see section 3.3), the error in droplet concentrations can still be kept within 10% for the whole series. This is highly acceptable, because an experimental uncertainty less than an order of magnitude is generally considered satisfactory in this kind of measurements.

Further, when the shock wave arrives back at the HPS endwall, there is a significant dip in the transmission. This can partly be attributed to the compression by the shock wave: the droplet concentration increases when the shock wave passes by, which causes more attenuation. Directly after the passage of the shock wave, the droplets start to evaporate owing to the temperature increase behind the shock. Therefore, the transmission signal immediately starts rising again. However, when droplet concentrations are negligibly low, the transmission dip can as well be observed at high pressures. The reason for this is not completely clear. The most plausible explanation is, that the signal disturbances are due to either deviations of the beam at the gradient in refraction index when the shock wave passes by, or to mechanical distortion of the tube windows. In

---

[1] The S/N-ratio is defined here as absolute decrease in transmission at the highest detectable Mie-peak divided by the absolute disturbance level.

both cases, the beam is refracted under some angle, so that the spot partly falls on the edge of the photodiode and the recorded intensity is lowered.

The scattered light shows, in comparison to low pressure experiments, only a small number of Mie-peaks. This is due to the droplet growth stage: at high pressures, the growth rate is limited by the diffusion rate of nonane through methane, which becomes smaller with increasing pressure. As a consequence, only a few peaks can be detected before the reflected shock wave brings the experiments to an end; measuring time can be enhanced by making the LPS longer. Agreement in shape between theoretical and experimental Mie-patterns remains very good at high pressures, as can be seen in figure 4.3. In
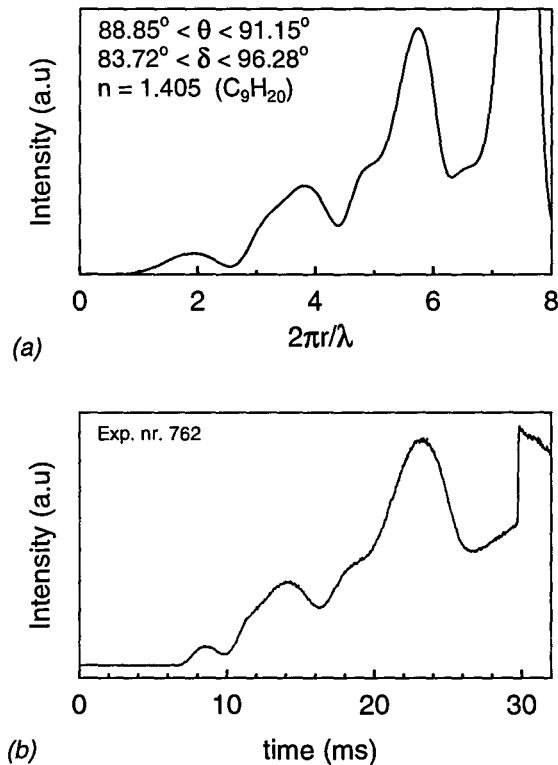
Figure 4.3: (a) Theoretical Mie-pattern for relevant experimental conditions as a function of reduced droplet radius and (b) Experimentally measured Mie-pattern as a function of time for the example experiment.

figure 4.3(b) the effect of the compression by the returning shock wave can clearly be recognized: first there is an increase in scattered intensity due to the higher droplet concentration behind the shock, but then the intensity starts falling again because of the gradual evaporation of droplets.

35

## 4.3 Results on $n$-nonane/methane

In figures 4.4 through 4.9, results of the nucleation experiments on the mixture $n$-nonane/methane are plotted. Results for the two methods of obtaining the molar fraction $y_v$ are represented in separate graphs. Numerical values of the experimentally determined parameters for each experiment can be found in appendix C.



Figure 4.4: *Results of nucleation measurements on n-nonane/methane(2.5). Supersaturation S calculated according to sampling method. Included are theoretical values at p = 19 bar and T = 241 K for both the binary classical nucleation theory (solid line) and the unary classical nucleation theory (dashed line).*



Figure 4.5: *Results of nucleation measurements on n-nonane/methane(2.5). Supersaturation S calculated according to growth method. Included are theoretical values at p = 19 bar and T = 241 K for both the binary classical nucleation theory (solid line) and the unary classical nucleation theory (dashed line).*

36

For the first series (figures 4.4 and 4.5), nucleation pressures are all within a small range around 19 bar; temperatures are close to 241 K. Values predicted by the binary classical nucleation theory (BCNT) described in chapter 2 for $p = 19$ bar and $T = 241$ K are also included. Moreover, to show the essential difference of the BCNT in comparison with the simple one-component classical nucleation theory (UCNT) for $n$-nonane with an inert carrier gas, results of the latter are also shown for the same $(p, T)$-conditions. Care should be taken while interpreting these graphs: part of the deviation between the two theories may be due to the use of different fits for the equilibrium density and the surface tension.
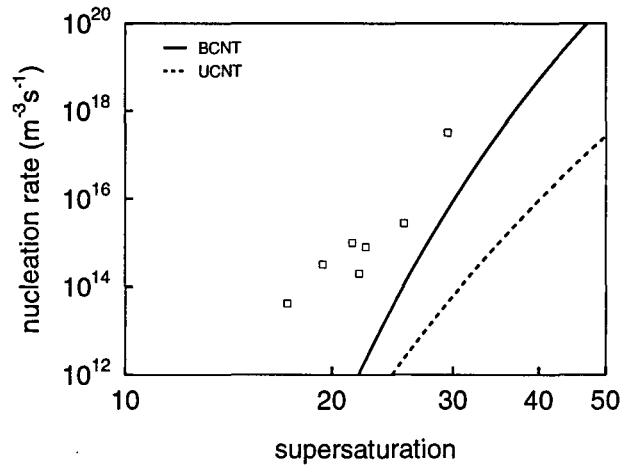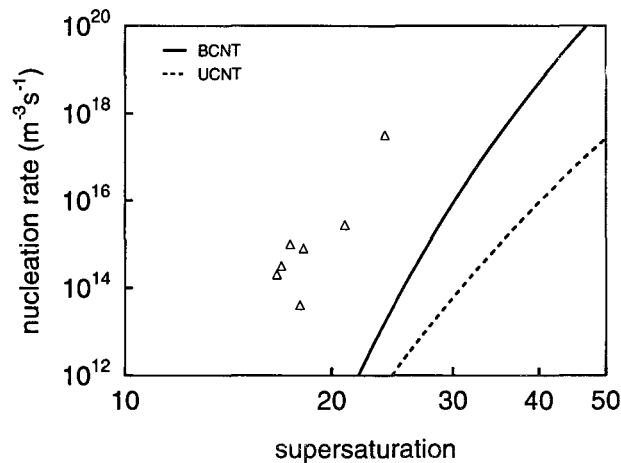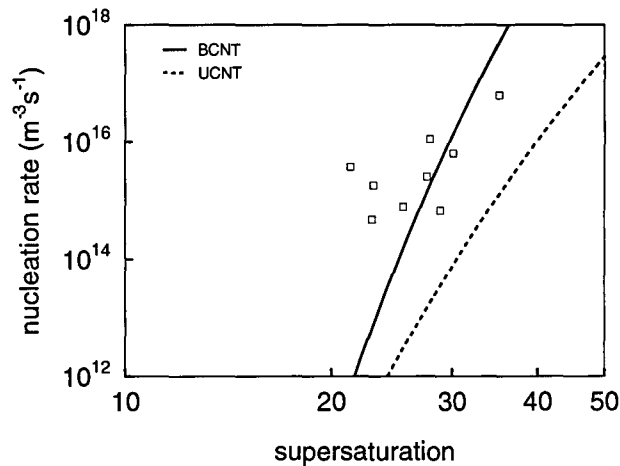


Figure 4.6: *Results of nucleation measurements on n-nonane/methane(4.5). Supersaturation S calculated according to sampling method. Included are theoretical values at p = 20 bar and T = 240 K for both the binary classical nucleation theory (solid line) and the unary classical nucleation theory (dashed line).*

Results for a series of experiments with condensation pressures close to 20 bar and condensation temperatures near 240 K are represented in the same way as above in figures 4.6 and 4.7. During this series, use was made of – relatively expensive – methane 4.5 (methane fraction larger than 0.99995) in the HPS. The series in figures 4.4 and 4.5 was done with – much cheaper – methane 2.5 (methane fraction larger than 0.995). No differences between the two series can be noticed that could have anything to do with the difference in pureness. Moreover, estimates indicate that the influence of the impurities (for the larger part being ethene and hydrogen) on the temperature decrease during expansion is negligible. Therefore, it turns out that methane 2.5 is sufficiently pure for the present purpose.

In the LPS, a mixture of 60% nitrogen and 40% hydrogen is used. This mixture is cheaper than methane and has nearly acoustical impedance, so that the resulting pressure history at the HPS endwall is nearly the same.

Figures 4.8 and 4.9 show the results of measurements with condensation pressures around 40 bar and temperatures around 241 K.

Figure 4.7: *Results of nucleation measurements on n-nonane/methane(4.5). Supersaturation S calculated according to growth method. Included are theoretical values at $p = 20$ bar and $T = 240$ K for both the binary classical nucleation theory (solid line) and the unary classical nucleation theory (dashed line).*



Figure 4.8: *Results of nucleation measurements on n-nonane/methane(4.5). Supersaturation S calculated according to sampling method. Included are theoretical values at $p = 40$ bar and $T = 241$ K for both the binary classical nucleation theory (solid line) and the unary classical nucleation theory (dashed line).*
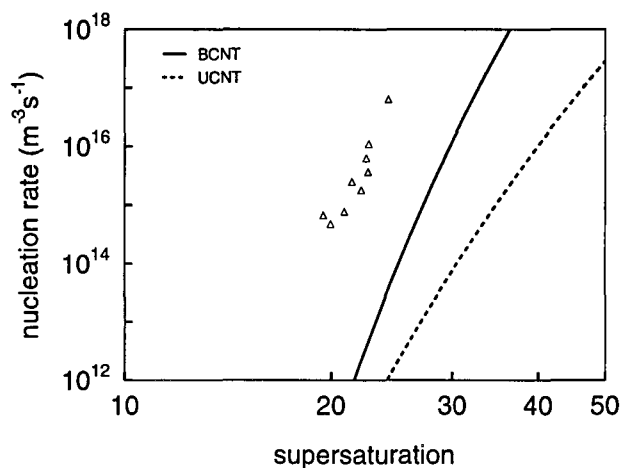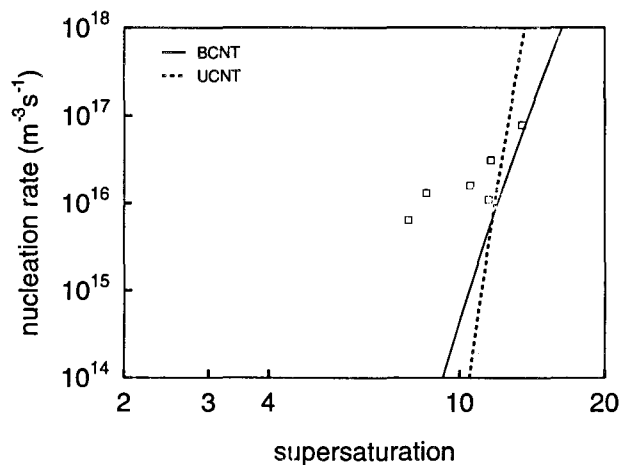
Figure 4.9: *Results of nucleation measurements on n-nonane/methane(4.5). Supersaturation $S$ calculated according to growth method. Included are theoretical values at $p = 40$ bar and $T = 241$ K for both the binary classical nucleation theory (solid line) and the unary classical nucleation theory (dashed line).*
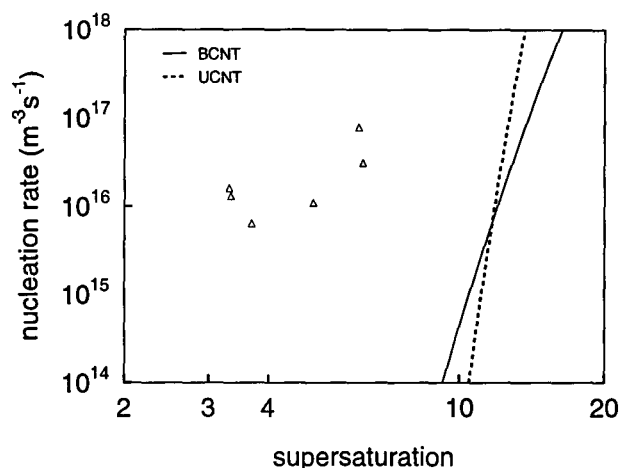
It is clear from figures 4.4 through 4.9 that with increasing pressure, the value of supersaturation that is needed to obtain a certain nucleation rate decreases. This need not be a real gas effect, however: it may as well be due to the definition of supersaturation. The equilibrium molar fraction of nonane increases with pressure, so that the same molar density of nonane at a higher total pressure corresponds to a lower supersaturation. In order to obtain a representation that does not have this interpretation problem, nucleation rates for the 20 bar and 40 bar series are plotted as a function of nonane density in figures 4.10 (sampling method) and 4.11 (growth method). Molar nonane densities are computed from the measured molar fraction and the condensation pressure and temperature using the RKS equation. Again, theoretical values according to both binary and unary theories are plotted.

All experimental points according to the growth method approximately fall on the same line. The low pressure data of Wagner and Strey [12] also appear to fit well on this line. The same holds for recent experiments by Looijmans at condensation pressures of 10 bar and 30 bar [13]. This could be an indication of the absence of real gas effects. However, in view of the large uncertainty in the composition of the mixture and the small number of experiments performed up to now, no final conclusion can be drawn concerning the importance of these effects in the nucleation behaviour of the mixture under consideration.

The two methods of determining the composition give systematically different results: the growth method yields smaller nonane fractions than the sampling method, thus smaller supersaturations. The reliability of both methods is further discussed in section 4.5. When we assume that the growth method is correct, experimental nucleation rates are roughly a factor $10^5$ higher than predicted by one component classical

39

Figure 4.10: *Results of nucleation measurements on n-nonane/methane represented as a function of the partial molar density of nonane. Molar nonane fraction calculated according to sampling method. Included are theoretical values at T = 240 K for both the binary classical nucleation theory (solid lines) and the unary classical nucleation theory (dashed lines).*



Figure 4.11: *Results of nucleation measurements on n-nonane/methane represented as a function of the partial molar density of nonane. Molar nonane fraction calculated according to growth method. Included are theoretical values at T = 240 K for both the binary classical nucleation theory (solid lines) and the unary classical nucleation theory (dashed lines). The results of n-nonane/argon experiments are added to show the influence of carrier gas.*

40

theory. The same deviation has also been observed for low pressures [12], which could again indicate that no real gas effects are present in the nucleation behaviour of the methane/nonane mixture.

## 4.4 Results on n-nonane/argon

In this section, attention is paid to the results of the nucleation experiments on the mixture n-nonane/argon. Numerical values of the experimental parameters are again listed in appendix C.



Figure 4.12: *Results of nucleation measurements on n-nonane/argon. Supersaturation S calculated according to sampling method. Included are theoretical values at p = 20 bar and T = 240 K for both the binary classical nucleation theory (solid line) and the unary classical nucleation theory (dashed line).*

In figures 4.12 and 4.13 the results are graphically represented, again including theoretical results for both BCNT and UCNT, at $p = 20$ bar and $T = 240$ K (average values for this series).

These experiments are shown as a function of nonane molar density in figure 4.14. The points according to the sampling method again show a large scatter. The growth method shows a line of experimental points lying to the left of the nonane/methane line in figure 4.11. This could be an indication of the presence of real gas effects in the nonane/methane mixture: since the equilibrium nonane density in the latter mixture is about 30% higher than in the nonane/argon mixture at the pressure and temperature under consideration (according to the RKS equation), higher nonane densities are required to obtain a certain nucleation rate. Still, care should be taken while interpreting the results in view of the small number of experiments performed up to now and the large uncertainty in composition.

A closer numerical examination of the nonane/argon mixture shows the following. At $T = 240$ K, the equilibrium fraction of argon in the liquid is about half as large as
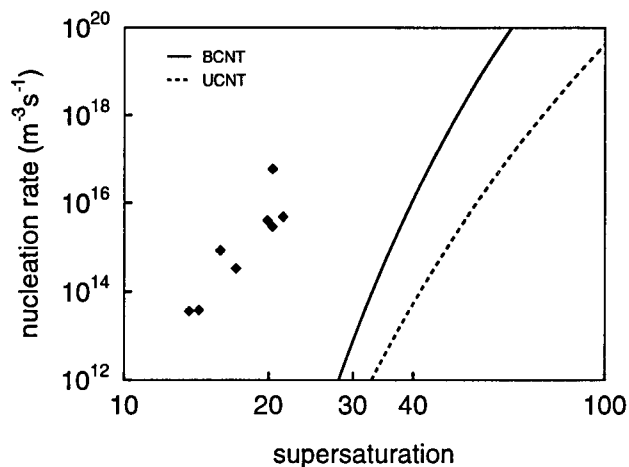
Figure 4.13: *Results of nucleation measurements on n-nonane/argon. Supersaturation S calculated according to growth method. Included are theoretical values at p = 20 bar and T = 240 K for both the binary classical nucleation theory (solid line) and the unary classical nucleation theory (dashed line).*
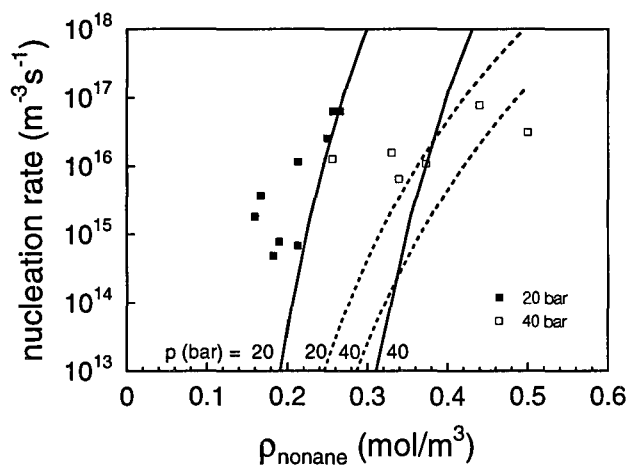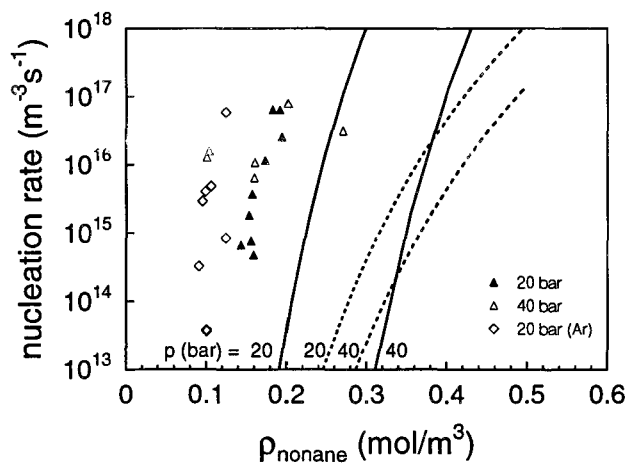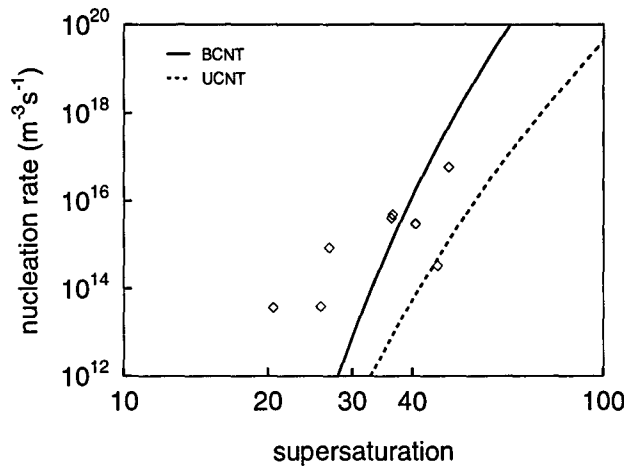

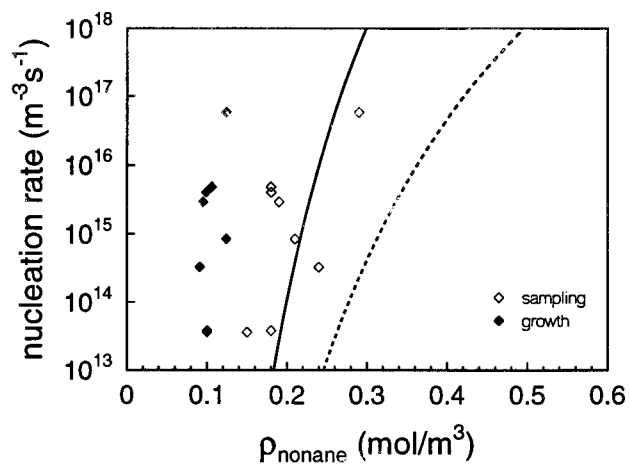
Figure 4.14: *Results of nucleation measurements on n-nonane/argon represented as a function of the partial molar density of nonane, according to both methods of composition determination. Included are theoretical values at T = 240 K and p = 20 bar for the binary classical nucleation theory (solid line) and the unary classical nucleation theory (dashed line).*

42

the equilibrium methane liquid fraction in the other mixture, but certainly not equal to zero. The surface tension lowering effect is as well present for argon, but it is less drastic than for methane. The solubility of nonane in the vapour phase again increases with pressure, as was the case for the nonane/methane mixture. Thus, argon gas can certainly *not* be considered as ideal, in the sense that it would only raise the pressure and not participate in the nucleation process. The fact that argon is chemically inert turns out not to be relevant here. Nevertheless, real gas effects – if present – are expected to be less important than in the nonane/methane case.

For comparison with nucleation in the absence of real gas effects, it seems a better idea to take a gas that is much further from its critical point at nucleation conditions, for instance helium or hydrogen gas. Only for this kind of gases, ideal behaviour in the above described sense can reasonably be expected, given the important role of the reduced temperature $T/T_c$ in the thermodynamic properties relevant for the nucleation process.

## 4.5   Experimental uncertainty

In this section, the experimental uncertainties involved in the nucleation experiments are analyzed. Moreover, the influence of these uncertainties on the interpretation of the comparison to the model in the previous sections is discussed.

The aim of the experiments on binary nucleation is, of course, to determine the relationship $J = J(p, T, y_v)$. All four of these quantities have their own experimental uncertainties.

Although $J$ is the most important quantity in the above relation, the error in its experimental value $J_{exp}$ is not much of a problem. $J_{exp}$ is obtained by dividing the measured droplet concentration in the nucleation pulse by the time duration of the pulse. The error in droplet concentrations due to the disturbances in the transmission signal at high pressures (see section 4.2) is at most 10%. The time duration $\Delta t$ of the pulse can also be determined within an accuracy of 10%, even for the least ideal pressure dips.[2] This comes down to an error of about 15% in nucleation rates, which can be considered small in view of the orders-of-magnitude scale that is commonly used in work on nucleation.

Another quantity that can easily be measured accurately is the pressure $p$. The initial (static) pressure and the dynamic pressure are both measured with a relative error (uncertainty) of about 0.5%.

A detailed analysis shows that the resulting absolute error in the condensation temperature is 0.6 K, provided that the assumption of isentropicity of the expansion is valid and that the equation of state of methane is perfectly known. The first assumption must be reasonable on the millisecond timescale of the nucleation experiments. Secondly, the

---

[2]This time duration should not be confused with the effective duration $\Delta t_{eff}$ introduced in appendix B, which can differ from $\Delta t$ by a factor 2.

equation that is used for calculation of the temperature of methane during the isentropic expansion, is reported to give an error of at most 0.2 K/MPa [14], being 0.8 K for an expansion from about 8 to 4 MPa (80 to 40 bar). The resulting total experimental error in the calculated temperature adds up to about 1 K.

For argon, the temperature is calculated according to the RKS equation of state. Results differ from ideal gas calculations only by a few hundreds of a Kelvin. The total experimental error in the temperature for argon is expected to be smaller than 1 K.

The largest experimental uncertainty is found in the molar nonane fraction $y_v$. For $n$-nonane/methane, the difference between the two methods of determining vapour fractions is about 25%; for $n$-nonane/argon, the difference can even be somewhat larger than a factor 2! This uncertainty adds up to the uncertainty in equilibrium molar concentration of about 10% (caused by the uncertainty in the condensation temperature of about 1 K). In order to make a final quantitative comparison between the experimental results and the model results it is necessary to reduce the experimental uncertainty, for example by deciding upon the reliability of either of the two methods applied to determine the concentration. At this moment, the accuracy of the sampling technique is not yet satisfactory but could probably be improved to give more reliable results. At the same time the validity of the growth model at high pressures should be verified independently. For the moment, the results obtained with the growth model give – somewhat intuitively – more confidence, since the scatter in the experimental points is less.

# Chapter 5

# Conclusions and recommendations

The investigation described in this report has dealt with the homogeneous condensation of binary real gas mixtures at high pressures. As far as the theoretical part is concerned, the aim of the study has been to revise the Binary Classical Nucleation Theory (BCNT) and its numerical implementation for real gases. Experimentally, the emphasis has been on the development of high pressure nucleation experiments using an expansion shock tube. The first few series of experiments of this kind have been performed, concerning the mixtures $n$-nonane/methane and $n$-nonane/argon.

A thermodynamic model for the formation free energy of clusters that accounts for real gas effects by using the Redlich-Kwong-Soave equation of state was implemented in the BCNT. The pioneering work of Hofmans in this field [15] has been refined and extended. The procedure he used for determining the saddle point position turned out to be thermodynamically inconsistent, and has been replaced by a method consisting of directly solving the Kelvin equations.

With the corrected model, nucleation rates were computed for the mixture under consideration as a function of pressure, temperature and molar nonane fraction. Results show that real gas effects can be expected to have a strong effect on the nucleation behaviour. For a fixed temperature and supersaturation, the methane content of the critical cluster increases approximately linearly with total pressure. As a consequence, the surface tension is significantly lowered, resulting in an increase in nucleation rate of several orders of magnitude for a 10 bar pressure increase.

An important point of concern remains that the surface tension of droplets is calculated using a fit on stable – flat surface – equilibrium values. The accuracy of this method in predicting the surface tension of the critical nucleus (metastable equilibrium, curved surface) must be doubted. Recent theories, like those of Dillman and Meier [16], Delale and Meier [17], and Kalikmanov and Van Dongen [18], do take into account the curvature of the droplet surface, but still need equilibrium surface tensions as their input. Solutions to this problem may come from molecular dynamics or Monte Carlo simulations of surface tension, recently being reported in literature.

Indeed it seems that the Classical Theory – strongly pending on the capillarity approximation – has reached its final stage: in order to proceed theoretically, information on a molecular scale becomes indispensable. However, a simulation of the nucleation process as a whole is still reported to be impossible for mainly two reasons. First, in order to simulate a system with a reasonable number of molecules (so that at least

one droplet would be formed within a human time scale) incredible amounts of computing time would be needed [19]. Second, these methods require accurate knowledge of intermolecular potentials, which is not or hardly available even for relatively simple molecules like the lower alkanes.

The expansion shock tube setup for measuring nucleation rates and droplet growth rates has been adapted to high pressure experiments. Droplet concentrations and sizes have been determined by a method based on transmitted light attenuation and 90° Mie-scattering. The scattering method remains very useful at high pressures. The attenuated beam becomes subject to rather severe disturbances at these circumstances. Only when droplet concentrations are sufficiently high, this method can still be used in the present setup. However, by calibrating the scattered light to such a high concentration experiment, droplet concentrations can still be accurately measured below the region where the attenuation method applies. Nucleation rates ranging from $10^{13}$ m$^{-3}$s$^{-1}$ up to $10^{18}$ m$^{-3}$s$^{-1}$ can be measured with the described setup. The overall accuracy in $J$ is better than 20%. A closer examination of the disturbances in the transmission signal at high pressures might further reduce this error.

The thermodynamic state during the nucleation pulse is obtained as an average between begin and end points. A more objective method, consisting of an integration over the pulse, has been proposed. The thermodynamic state during an experiment is calculated from the pressure, assuming that the expansion can be considered isentropic. Direct measurements of temperature at the endwall of the tube turned out to be extremely difficult in view of the stagnant state of the fluid at the endwall. It is worthwile investigating the possibility of measuring temperature somewhere in the flow, thereby correcting for the difference in gas velocity with respect to the situation at the endwall.

The main experimental concern is the determination of the initial gas composition. Two methods have been used for this purpose: one method based on gas sampling (selective adsorption and gas chromatography) and the other based on simulations of droplet growth rates. The latter requires less effort, but has no direct experimental justification. The sampling method is still being developed, and is expected to be rather inaccurate in its present form. Molar fractions obtained by the two methods in some cases differed by more than a factor 2, the sampling method in all cases yielding the larger fraction. The growth method seems to be more reliable because of the generally observed smaller scatter between data points of a series. However, the reliability of the underlying growth model at high pressures needs to be checked independently before presenting it as an accurate tool to determine molar fractions.

It seems a promising alternative to make the sampling technique more direct by leading the gas sample directly into a gas chromatographer. Methods of reducing the pressure without changing the composition of the sample on its way to the chromatographer are currently under consideration.

The first high pressure nucleation measurements performed with the described setup are reported. Nucleation rate measurements on the mixture $n$-nonane/methane show

that the value of supersaturation required to obtain a certain nucleation rate decreases with increasing pressure. Although predicted by the binary model, this need not be a real gas effect. It could be due to the definition of supersaturation, since the reference (equilibrium) molar fraction increases with increasing pressure. When nucleation rates are plotted as a function of partial nonane density, experimental points belonging to different pressures (ranging from 1 to 40 bar) appear to fall approximately on the same line (when the growth model is used to determine the composition of the mixture). This is in contradiction with the predictions of the binary nucleation model, and could be an indication of the absence of real gas effects in nucleation. Nevertheless, results for the $n$-nonane/argon mixture show a parallel line shifted to lower densities, which shows that there must be an influence of the gas component of the mixture on the nucleation behaviour of nonane.

However, because of the mentioned uncertainty in gas composition, care should be taken in interpreting experimental results at this stage of the investigation.

As a final conclusion, no differences were found in nucleation behaviour between methane 2.5 and the far more expensive methane 4.5. In view of the harsh economic times the Physics Department is going through, this can be wellcomed as good news.

# References

[1] F. Peters, *"A new method to measure homogeneous nucleation rates in shock tubes"*. Exp Fluids, **1**, 143 (1983)

[2] K.N.H. Looijmans, P.C. Kriesels and M.E.H. van Dongen, *"Gasdynamic aspects of a modified expansion-shock tube for nucleation and condensation studies"*. Exp. Fluids **15**, 61 (1993)

[3] A.J. Chorin, *"Random Choice Solution of Hyperbolic Systems"*. J. Comput. Phys. **22**, 517 (1976)

[4] H.J. Smolders, E.J.M. Niessen and M.E.H. van Dongen, *"The random choice method applied to non-linear wave propagation in gas-vapour-droplet mixtures"*. Comp. Fluids **21**, 63 (1992)

[5] C.A.M. Snoeijs, *"De optische karakterisering van nevels"*. Master's thesis TUE nr. R–1169–A (1992)

[6] H.C. van de Hulst, *"Light scattering by small particles"*. Wiley, New York (1981)

[7] K.N.H. Looijmans, *"Nucleatie en condensatie in binaire mengsels met alkanen"*. Master's thesis TUE nr. R–1072–A, (1990)

[8] M. Verschueren, private communication (1994)

[9] J.P.A.J. van Beeck, *"Een reëel druppelgroeimodel, belicht in een binair mengsel"*. Master's thesis TUE nr. R–1169–A (1992)

[10] G. Gyarmathy, Multiph. Sci. Techn. **1**, 99 (1982)

[11] R. van Schaijk, ????? (NADER IN TE VULLEN)

[12] P.E. Wagner and R. Strey, *"Measurements on homogeneous nucleation rates for n-nonane vapor using a two-piston expamsion chamber"*. J. Chem. Phys. **80**, 5266 (1984)

[13] K.N.H. Looijmans, private communication (1994)

[14] V.V. Sychev, V.A. Zagoruchenko, A.D. Kozlov, G.A. Spiridonov and V.A. Tsymarny, *"Thermodynamic properties of methane"*. National Standard Reference Data Service of the USSR. Springer Verlag, Berlin (1987)

[15] G.C.J. Hofmans, *"Homogeneous nucleation of real binary mixtures"*.
Master's thesis TUE nr. R–1232–A (1993)

[16] A. Dillmann and G.E.A. Meier, *"A refined droplet approach to the problem of homogeneous nucleation from the vapor phase"*.
J. Chem. Phys. **94**, 3872 (1991)

[17] C.F. Delale and G.E.A. Meier, *"A semiphenomenological droplet model of homogeneous nucleation from the vapor phase"*.
J. Chem. Phys. **98**, 9850 (1993)

[18] V.I. Kalikmanov and M.E.H. van Dongen, *"Semi-phenomenological kinetic theory of binary nucleation"*, submitted.

[19] H.M. Ellerby, C.L. Weakliem and H. Reiss, *"Toward a molecular theory of vapor-phase nucleation. Identification of the average embryo"*.
J. Chem. Phys. **95**, 9209 (1991)

[20] R.C. Reid, J.M. Prausnitz and B.E. Poling, *"The properties of gases and liquids"*.
McGraw-Hill Book Company, New York (1987)

[21] Y. Viisanen, R. Strey and H. Reiss, *"Homogeneous nucleation rates for water"*.
J. Chem. Phys. **99**, 4680 (1993)

# Appendix A

# Numerical code

The FORTRAN code in which the binary nucleation theory is implemented (originally written by G. Hofmans, modified by K. Looijmans and C. Luijten) consists of a hierarchy of subroutines. A block scheme of the program structure is found in figure A.1. The arrows denote data transport between subroutines and also show the positions of subroutines in the hierarchy.
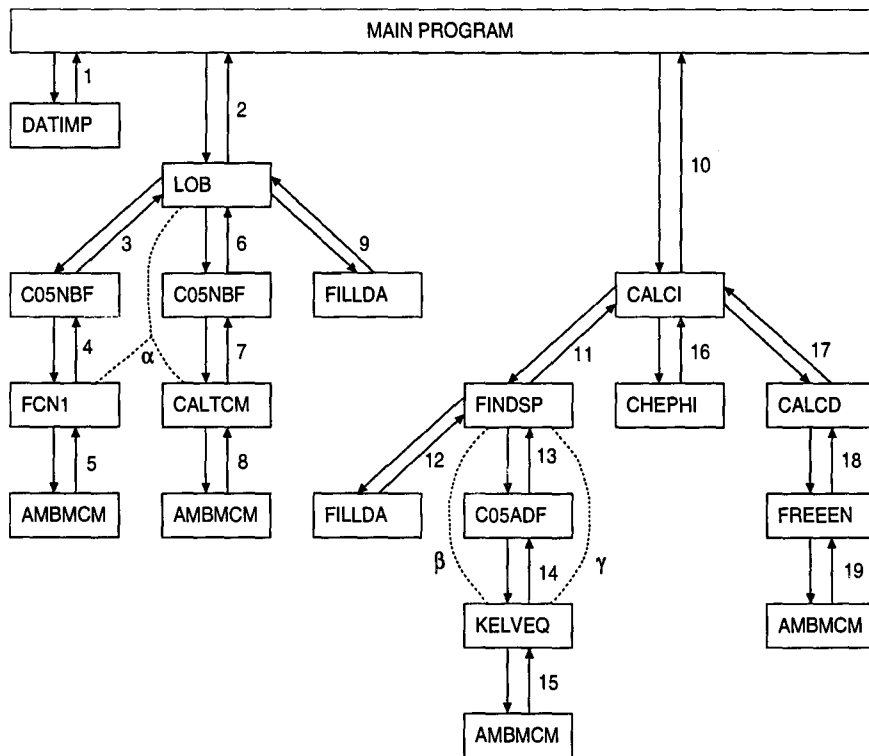
Figure A.1: *Block scheme of the numerical code that is used to calculate nucleation rates according to the model described in chapter 2. Arrows indicate data transport between subroutines; dashed lines denote common blocks (see text for an explanation of the symbols).*

In the following, the program subroutines are briefly described. Not included are functions that are called from several positions in the program to make calculations that are relatively straightforward, for instance calculations of molecular volumes and chemical potentials according to the RKS equation of state and of the surface tension according to the parachor method. More complete descriptions of subroutines and functions can be found in the program listing.[1]

| | |
|---|---|
| DATIMP | Imports the necessary data – composition of the mixture, pressure and temperature ranges – from the screen. |
| LOB | Calculates the equilibrium pressure for the given temperature range. In this way, calculations of nucleation rates can be restricted to the relevant region, i.e. inside the equilibrium lob. |
| FILLDA | Attaches numerical values to the program variables corresponding to material properties of the mixture's components that are chosen. Data are obtained from the book by Reid *et al.* [20]. |
| C05NBF | Standard routine from the FORTRAN NAG-library that determines the solution of a system of non-linear equations. |
| FCN1 | Is called by C05NBF in order to find the equilibrium pressure and composition of the liquid. This is done by equating chemical potentials in the vapour and the liquid for each component. |
| CALTCM | Is called by C05NBF in order to find the critical temperature of the vapour mixture according to the mixing rules of the RKS equation of state. |
| AMBMCM | Calculates the RKS parameters for the mixture. |
| CALCI | Calculates the nucleation rate. |
| FINDSP | Searches for the saddle point on the free energy surface by means of solving the Kelvin equations. |
| C05ADF | Standard routine from the FORTRAN NAG-library that determines the zero of a continuous function on a given interval. |
| KELVEQ | Is called by C05ADF in order to solve the Kelvin equation. |
| CHEPHI | Checks the angle of the nucleation current at the saddle point (calculated by function CALPHI). It is found correct if it leads to a maximum in the nucleation rate. |
| CALCD | Calculates the second derivatives of the free energy surface at the saddlepoint position. |
| FREEEN | Calculates the free energy of a droplet containing a given number of molecules of both components. |

---

[1]for a program listing, please contact the author.

To complete this program description, the data transport between subroutines is described in terms of variables that are either input to (i) or output from (o) a subroutine. Data streams are numbered from 1 through 19 in figure A.1; common blocks are denoted with greek symbols.

1  i: (nothing)
   o: COMP, YFRAC, TBEGIN, TEND, TSTEPS, PBEGIN, PEND, PSTEPS
2  i: COMP, YFRAC, TBEGIN, TEND, TSTEPS
   o: STOP, PEQ
3  i: FCN1, DIMEN, SOLVEC, XTOL, WWA, LWA, IFAIL
   o: SOLVEC, FVEC
4  i: N, X, IFLAG
   o: FVEC
5  i: YFRAC, TCMIX, R, PC, TC, M, OMEGA, ZRA, KIJ
   o: A, B, AM, BM, CM
6  i: CALTCM, DIMEN, TCM, TOL, WA, LWA, IFAIL
   o: TCM, DELTA
7  i: NUMEQ, TCMIX, IFLAG
   o: DIFF
8  i: YFRAC, TCMIX, R, PC, TC, M, OMEGA, ZRA, KIJ
   o: A, B, AM, BM, CM
9  i: COMP, YFRAC
   o: PC, TC, VC, M, OMEGA, ZRA, PARACH, KIJ, VP , EQUA
10 i: TBEGIN, TEND, TSTEPS, STOP, PBEGIN, PEND, PSTEPS, PEQ, COMP, YFRAC
   o: (nothing)
11 i: P, T, KLCRIT, COMP, Y
   o: KLCRIT, RESULT, M, SIGMASP
12 i: COMP, QY
   o: PC, TC, VC, M, OMEGA, ZRA, PARACH, KIJ, VP , EQUA
13 i: LBOUND, RBOUND, TOL, ETA
   o: IFAIL, X, KELVEQ
14 i: X
   o: X,KELVEQ
15 i: X, T, R, PC, TC, M, OMEGA, ZRA, KIJ
   o: A, B, AM, BM, CM
16 i: PHI, GXX, RAV, DAA, DAB, DBB, Y, T, M, RADIUS, VVAP
   o: OK
17 i: KLCRIT
   o: DAA, DAB, DBB, GSP, VVAP, RADIUS
18 i: KLCRIT
   o: GKL, OK, VV, R
19 i: Y, T, R, PC, TC, M, OMEGA, ZRA, KIJ
   o: A, B, AM, BM, CM

53

Common blocks:

$\alpha$  /FCN1IN/  T, YFRAC, R, NA, PC, TC, M, OMEGA, ZRA, KIJ

$\beta$  /CONSTA/  AM, BM, CM, PV, VV, T, R, NA, PARACH, Y, K, L,
PC, TC, M, OMEGA, ZRA, KIJ, SIGMA

$\gamma$  /KELVIO/  MUVAP, MULIQ, V, VL, C

# Integration over the nucleation pulse

In chapter 3 the determination of the thermodynamic state during the nucleation pulse was described. The disadvantage of the result being subject to some ambiguity was mentioned. In the following, a solution to this problem is presented.

The classical expression for the nucleation rate can be written in the following form:

$$J = J_0 \exp\{-A\varphi\}, \tag{B.1}$$

where

$$\varphi = \frac{\sigma^3}{T^3 \ln^2 S} \tag{B.2}$$

and

$$A = \frac{16\pi}{3} \frac{m^2}{\rho_l^2 k_B^3} \tag{B.3}$$

according to single component classical theory ($m$ is the molecular mass and $\rho_l$ the liquid density).
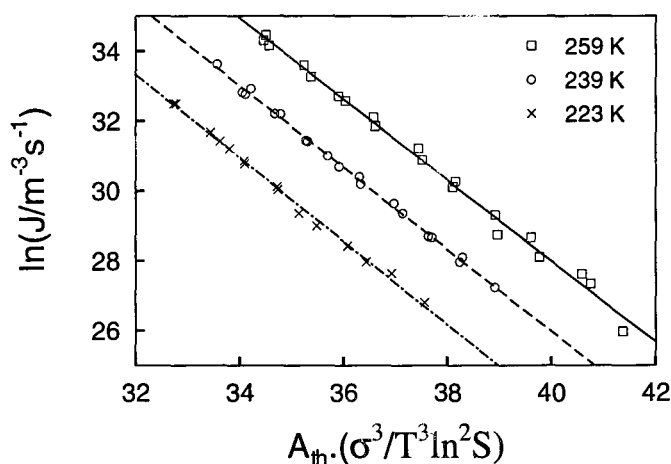


Figure B.1: *Variation of $J$ with the parameter $\varphi$ for water according to experimental data of Wagner and Strey. $A = 7.1 \cdot 10^{12}$ (averaged experimental value).*

The value of $A$ can as well be obtained from experimental data by plotting $\ln J$ versus $\varphi$. This has been done for water and nonane; results can be seen in figures B.1 and B.2.
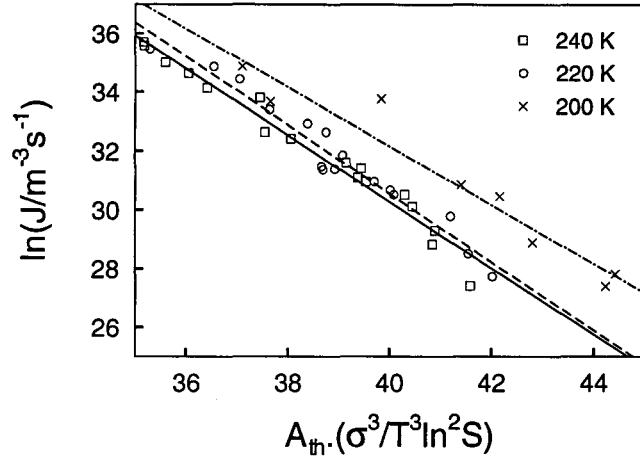
Figure B.2: *Variation of J with the parameter $\varphi$ for n-nonane according to experimental data of Viisanen, Strey and Heist. $A = 5.6 \cdot 10^{14}$ (averaged experimental value).*

For convenience, the theoretical values $A_{th}$ are used for scaling the horizontal axes. Data are from Wagner and Strey [12] and from Viisanen *et al.* [21], respectively.

Now, we choose the point of lowest pressure in the pulse as a reference point. Equation (B.1) transforms to

$$J = J_{ref} \exp\{A(\varphi_{ref} - \varphi)\} \tag{B.4}$$

where subscript "ref" denotes, of course, values in the reference point.

For one component condensation, it is easy to calculate $\varphi(t)$ for every point in the pressure dip using fits for $\sigma$ and for the saturation pressure $p_{sat}$ as a function of $T$. The behaviour of $\varphi$ (and thus $\ln J$) with $p$ (for constant entropy) turns out to be almost linear.

The total number density of droplets $n_{exp}$ follows from

$$n_{exp} = \int\limits_{dip} J \, dt = J_{ref} \int\limits_{dip} \exp\left\{A\left(\varphi_{ref} - \varphi(t)\right)\right\} \, dt, \tag{B.5}$$

in which the last integral can be recognized as the effective pulse duration $\Delta t_{eff}$. The value of $J_{ref}$ is now simply obtained as the ratio $n_{exp}/\Delta t_{eff}$.

The above method can be given the following interpretation. The pulse is modeled by a rectangular one with thermodynamic state $(p_{ref}, T_{ref})$ and duration $\Delta t_{eff}$ in such a way, that the total number density of droplets integrated over the pulse is equal to the experimentally observed number density. This comes down to exactly determining the experimental point $J_{ref}(p_{ref}, T_{ref}, y_v)$ without any ambiguity. Of course, this can be done for every other point of the dip, but this yields no extra information and makes the interpretation of the procedure less evident.

Implementation of this method becomes more difficult in a binary system, where a relationship like (B.1) does not exist. However, $\ln J$ can be linearized as a function of $p$ using binary theory, by numerically evaluating the derivative $\frac{\delta \ln J}{\delta p}\big|_s$ for an isentropic expansion.

First, a point $J(p, T, y_v)$ is calculated with $p$, $T$ and $y_v$ close to the experimental values. Then the pressure is raised by an amount $\delta p$; consequently, temperature changes isentropically by an amount approximately equal to $\left(\frac{\gamma-1}{\gamma}\right)\left(\frac{\delta p}{p}\right) T$. These new values will yield a nucleation rate with logarithm $(\ln J + \delta \ln J)$, so that the derivative is known, and equal to $\frac{\delta \ln J}{\delta p}$. By a relation similar to (B.5),

$$
n_{exp} = \int\limits_{dip} J \; dt = J_{ref} \int\limits_{dip} \exp\left\{\frac{\delta \ln J}{\delta p}\left(p(t) - p_{ref}\right)\right\} \; dt, \tag{B.6}
$$

the effective pulse duration can be determined. The only assumption that must be made, compared to the situation for one component, is that the numerically evaluated derivative $\frac{\delta \ln J}{\delta p}$ does not depend on the theory used. This seems to be justified for a small temperature range, because all known theories predict nearly the same linearized dependence of $J$ on supersaturation for fixed temperatures. An experimental verification for this method like figures B.1 and B.2 is not yet available because no high pressure nucleation data exist for the mixture under consideration.

# Tables of results

In this appendix relevant parameters of the nucleation experiments on the mixtures $n$-nonane/methane and $n$-nonane/argon are represented in tabular form. Nonane molar fractions have been determined both according to the gas sampling method and by using the growth model.

| Exp. nr. | $p_0$ (bar) | $T_0$ (K) | $p_{cond}$ (bar) | $T_{cond}$ (K) | $y_{eq}$ $\cdot\ 10^6$ |
|---|---|---|---|---|---|
| 760 | 40.12 | 294.3 | 18.7 | 242.3 | 9.30 |
| 761 | 42.78 | 297.7 | 19.1 | 242.6 | 9.57 |
| 762 | 43.69 | 297.3 | 18.8 | 239.9 | 7.46 |
| 763 | 43.99 | 298.0 | 19.5 | 242.3 | 9.33 |
| 764 | 43.81 | 296.6 | 18.4 | 237.8 | 6.11 |
| 765 | 44.04 | 297.5 | 19.8 | 242.8 | 9.78 |
| 767 | 43.83 | 297.0 | 19.5 | 241.8 | 8.92 |

| Exp. nr. | $y_{sample}$ $\cdot\ 10^4$ | $y_{growth}$ $\cdot\ 10^4$ | $S_{sample}$ | $S_{growth}$ | $J$ $(\mathrm{m^{-3}s^{-1}})$ |
|---|---|---|---|---|---|
| 760 | 1.6 | 1.67 | 17.2 | 18.0 | $4.1 \cdot 10^{13}$ |
| 761 | 2.1 | 1.59 | 21.9 | 16.6 | $2.0 \cdot 10^{14}$ |
| 762 | 1.9 | 1.56 | 25.5 | 20.9 | $2.8 \cdot 10^{15}$ |
| 763 | 2.0 | 1.62 | 21.4 | 17.4 | $1.0 \cdot 10^{15}$ |
| 764 | 1.8 | 1.46 | 29.5 | 23.9 | $3.2 \cdot 10^{17}$ |
| 765 | 1.9 | 1.65 | 19.4 | 16.9 | $3.2 \cdot 10^{14}$ |
| 767 | 2.0 | 1.62 | 22.4 | 18.2 | $8.1 \cdot 10^{14}$ |

Table C.1: *Results of the measurements on the mixture n-nonane/methane(4.5) at condensation pressures around 19 bar and temperatures around 241 K. Included are molar fractions and supersaturations according to both the gas sampling method and the method based on droplet growth rate.*

| Exp. nr. | $p_0$ (bar) | $T_0$ (K) | $p_{cond}$ (bar) | $T_{cond}$ (K) | $y_{eq} \cdot 10^6$ |
|---|---|---|---|---|---|
| 727 | 43.98 | 294.2 | 19.6 | 239.29 | 7.08 |
| 728 | 44.10 | 293.2 | 19.6 | 238.38 | 6.51 |
| 729 | 44.20 | 294.1 | 19.9 | 239.74 | 7.41 |
| 730 | 43.99 | 294.2 | 19.6 | 239.21 | 7.03 |
| 731 | 44.90 | 295.7 | 19.7 | 239.44 | 7.19 |
| 735 | 45.58 | 297.4 | 19.8 | 240.53 | 7.96 |
| 740 | 44.59 | 295.1 | 20.2 | 241.01 | 8.35 |
| 741 | 44.08 | 294.4 | 19.6 | 239.32 | 7.10 |
| 742 | 44.69 | 295.1 | 19.6 | 239.03 | 6.93 |

| Exp. nr. | $y_{sample} \cdot 10^4$ | $y_{growth} \cdot 10^4$ | $S_{sample}$ | $S_{growth}$ | $J$ $(\mathrm{m^{-3}s^{-1}})$ |
|---|---|---|---|---|---|
| 727 | 1.8 | 1.48 | 25.4 | 20.9 | $7.7 \cdot 10^{14}$ |
| 728 | 1.5 | 1.44 | 23.0 | 22.1 | $1.8 \cdot 10^{15}$ |
| 729 | 1.7 | 1.48 | 22.9 | 20.0 | $4.8 \cdot 10^{14}$ |
| 730 | 1.5 | 1.59 | 21.3 | 22.6 | $3.7 \cdot 10^{15}$ |
| 731 | 2.0 | 1.63 | 27.8 | 22.6 | $1.1 \cdot 10^{16}$ |
| 735 | 2.4 | 1.79 | 30.2 | 22.5 | $6.3 \cdot 10^{15}$ |
| 740 | 2.3 | 1.79 | 27.5 | 21.4 | $2.5 \cdot 10^{15}$ |
| 741 | 2.5 | 1.72 | 35.2 | 24.2 | $6.3 \cdot 10^{16}$ |
| 742 | 2.0 | 1.35 | 28.9 | 19.5 | $6.7 \cdot 10^{14}$ |

Table C.2: *Results of the measurements on the mixture n-nonane/methane(2.5) at condensation pressures around 20 bar and temperatures around 240 K. Included are molar fractions and supersaturations according to both the gas sampling method and the method based on droplet growth rate.*

| Exp. nr. | $p_0$ (bar) | $T_0$ (K) | $p_{cond}$ (bar) | $T_{cond}$ (K) | $y_{eq}$ $\cdot 10^5$ |
|---|---|---|---|---|---|
| 750 | 84.75 | 295.2 | 41.1 | 243.87 | 1.81 |
| 751 | 85.36 | 295.4 | 39.7 | 241.25 | 1.41 |
| 752 | 85.06 | 294.6 | 39.8 | 240.95 | 1.39 |
| 753 | 87.27 | 295.8 | 39.8 | 240.37 | 1.33 |
| 754 | 86.97 | 295.2 | 39.8 | 239.98 | 1.29 |
| 755 | 87.26 | 295.8 | 41.7 | 243.41 | 1.79 |

| Exp. nr. | $y_{sample}$ $\cdot 10^4$ | $y_{growth}$ $\cdot 10^4$ | $S_{sample}$ | $S_{growth}$ | $J$ $(m^{-3}s^{-1})$ |
|---|---|---|---|---|---|
| 750 | 2.1 | 1.14 | 11.6 | 6.30 | $3.1 \cdot 10^{16}$ |
| 751 | 1.9 | 0.87 | 13.5 | 6.17 | $7.8 \cdot 10^{16}$ |
| 752 | 1.6 | 0.69 | 11.5 | 4.96 | $1.1 \cdot 10^{16}$ |
| 753 | 1.4 | 0.44 | 10.5 | 3.31 | $1.6 \cdot 10^{16}$ |
| 754 | 1.1 | 0.43 | 8.53 | 3.33 | $1.3 \cdot 10^{16}$ |
| 755 | 1.4 | 0.66 | 7.82 | 3.69 | $6.4 \cdot 10^{15}$ |

Table C.3: *Results of the measurements on the mixture n-nonane/methane(4.5) at condensation pressures around 40 bar and temperatures around 241 K. Included are molar fractions and supersaturations according to both the gas sampling method and the method based on droplet growth rate.*

| Exp. nr. | $p_0$ (bar) | $T_0$ (K) | $p_{cond}$ (bar) | $T_{cond}$ (K) | $y_{eq}$ $\cdot 10^6$ |
|---|---|---|---|---|---|
| 770 | 34.25 | 297.2 | 20.5 | 241.9 | 6.99 |
| 771 | 33.65 | 297.1 | 20.4 | 243.1 | 7.82 |
| 772 | 34.05 | 297.9 | 19.9 | 240.4 | 6.09 |
| 774 | 34.55 | 299.4 | 19.5 | 238.2 | 4.95 |
| 775 | 34.35 | 298.3 | 20.5 | 242.4 | 7.32 |
| 777 | 34.85 | 298.3 | 19.9 | 238.3 | 4.98 |
| 780 | 34.65 | 298.9 | 19.8 | 238.8 | 5.32 |
| 781 | 34.55 | 299.4 | 19.4 | 237.6 | 4.67 |

| Exp. nr. | $y_{sample}$ $\cdot 10^4$ | $y_{growth}$ $\cdot 10^4$ | $S_{sample}$ | $S_{growth}$ | $J$ $(m^{-3}s^{-1})$ |
|---|---|---|---|---|---|
| 770 | 1.8 | 1.00 | 25.8 | 14.3 | $3.8 \cdot 10^{13}$ |
| 771 | 2.1 | 1.24 | 26.9 | 15.9 | $8.5 \cdot 10^{14}$ |
| 772 | 2.9 | 1.24 | 47.6 | 20.4 | $5.8 \cdot 10^{16}$ |
| 774 | 1.8 | 1.06 | 36.4 | 21.4 | $4.8 \cdot 10^{15}$ |
| 775 | 1.5 | 1.00 | 20.5 | 13.7 | $3.6 \cdot 10^{13}$ |
| 777 | 1.8 | 0.99 | 36.1 | 19.9 | $4.0 \cdot 10^{15}$ |
| 780 | 2.4 | 0.91 | 45.1 | 17.1 | $3.3 \cdot 10^{14}$ |
| 781 | 1.9 | 0.95 | 40.7 | 20.3 | $2.9 \cdot 10^{15}$ |

Table C.4: *Results of the measurements on the mixture n-nonane/argon. Included are molar fractions and supersaturations according to both the gas sampling method and the method based on droplet growth rate.*

# Dankwoord

Op deze plaats wil ik graag iedereen bedanken die heeft bijgedragen aan het tot stand komen van dit afstudeerwerk. Dit betreft in het bijzonder Karel Looijmans, mijn afstudeerbegeleider die zich met nimmer aflatende ijver van deze taak heeft gekweten (zelfs tijdens het pingpongen!).

Daarnaast zijn er vele verhelderende gesprekken over theoretische aspecten geweest met Geert Hofmans, Vitali Kalikmanov en Marcel Muitjens waarvoor ik hen zeer erkentelijk ben.

De revolutionaire hogedruk-metingen waarvan in dit verslag gewag wordt gemaakt hebben hun bestaan voor een groot deel te danken aan de vakbekwaamheid van Harm Jager en Jan Willems, de spreekwoordelijke rotsen in de branding van de experimentele fysica in de kelder van W&S.

Tot slot gaat mijn dank uit naar Rini van Dongen voor de uitstekende begeleiding tijdens het afgelopen jaar en voor het in mij gestelde vertrouwen voor de toekomst. Ik hoop in de komende periode een bijdrage te kunnen leveren aan de prima sfeer die ik binnen de groep Gasdynamica/Aeroakoestiek heb mogen ervaren.